5-2015

Synthesis, functionalization, and characterization of metallic and organic nanoparticles for biomedical applications

Christopher Brian Sylvester

Synthesis, functionalization, and characterization of metallic and organic nanoparticles for biomedical applications

by

Christopher Brian Sylvester

Undergraduate honors thesis under the direction of

Dr. Daniel J Hayes

Department of Biological & Agricultural Engineering

Submitted to the LSU Honors College in partial fulfillment of
the Upper Division Honors Program.

May, 2015

Louisiana State University
& Agricultural and Mechanical College
Baton Rouge, Louisiana

DEDICATION

I would like to dedicate this thesis to the faculty and staff of the Department of Biological & Agricultural Engineering at LSU. At some point each and every one of you has played a role in my growth as a professional and a researcher. Because of you I have achieved things I could never have imagined only four years ago.

ACKNOWLEDGEMENTS

Thanks to my parents for always being there and supporting me in my undertakings. I would like to acknowledge my research advisors, Dr. Daniel Hayes, Dr. Cristina Sabliov, and Dr. Carlos Astete for working with me throughout the years and teaching me how to be a researcher. I would like to thanks the graduate staff of both the Hayes and Sabliov lab, especially Nick Totaro, Amar Quereshi, Alyson Moll, Cong Walker, and Thanida Chuacharoen. At some point I have come to each of you for help, and you gave it graciously. I would like to acknowledge the work my senior design team, Kaity Addison, Allison Bosworth, Kailin McClure, and Megan Nalewaik, contributed to the last chapter. I could not have done it without you. Katie Hogan was one of the best research partners I could have asked for to learn and grow with in my time as a student. Finally and most of all, I would like to thank Mark Hoppens. You always believed in me and pushed me to do my best, and I could not have achieved what I did without your mentorship.

Table of Contents

PREFACE

This thesis is the compilation of four years of undergraduate research. I have reported all of the studies here in their entirety for completeness, but while I contributed to each of them, I was not necessarily the lead researcher. This report not only tells the stories of the studies presented but also of my growth as a researcher. The first study was my initial exposure to research. Here I learned the basic skills that would carry me throughout my undergraduate research. The antimicrobial silver nanoparticle study was my first authorship on publication and really set me on my path of taking research as a career. The final study was my first time leading a research project. I undertook it as group leader of my senior design team, and I am hopeful that it will materialize into my premier first-author publication.

ABSTRACT

Advancements in the synthesis and control of nanomaterials has created a boom in the amount of research being conducted with nanoparticles. Size control is one of the most basic and important aspects of nanoparticles, and size alone can greatly influence the properties of the particles. The materials which make up nanoparticles also play a large role in defining their characteristics. Two types of nanoparticles, metallic and organic are examined here. Metallic nanoparticles offer increased stability of the nanoparticles and associated molecules in the body. Their surfaces and easily be functionalized with ligands to increase solubility or provide unique characteristics. Iron and silver nanoparticles are used here. Iron can be used as an MRI contrast agent, and silver offers broad spectrum antimicrobial qualities. Additionally, because of its noble metal characteristics thiol bonds can easily be reduced onto silver. This fact is taken advantage of by using the thiol group on the end of CSA-124, a ceragenin to which shows powerful antimicrobial qualities to attach it to the silver surface of nanoparticles. The attachment of CSA-124 offers spatial selectivity towards *S.* aureus. Organic nanoparticles offer the benefits of reduced cytotoxicity and being easily degradable by the body. Zein, a well-characterized protein found in corn, is used to entrap docosahexaenoic acid, and omega-3 fatty acid which has been implicated in increased recovery time after brain injuries. All particles are characterized both physically and their interactions with biological systems. Their unique properties are examined and evaluated for the possibility of their further testing for use as biomedical agents.

CHAPTER 1. INTRODUCTION

1.1 The Clinical Need for New Antimicrobials

With the rise in numbers and persistence of antibiotic-resistant strains of bacteria, there has been an increasing need for new forms of antibiotics. However, progress in this area of drug development has been lagging compared to broader arena of medicine. Advancements that are made are often chemical variations of older antibiotics, and while more powerful than the last generation, resistant strains arise rapidly after the drug begins circulation. Another problem arises when using more powerful versions of antibiotics: broad activity against native, beneficial microbes. For example, the reduction of native fauna in the gut can further complicate recovery from a serious infection as a result of gastrointestinal dysfunction or secondary infection from an opportunistic pathogen. One study estimates the cost of *C. difficile,* and opportunistic gut pathogen, at $1.1 billion per year in the United States [1]. These complications can be especially troublesome when and individual has been infected with an antibiotic-resistant strain or is immunocompromised. As a response to these issues with traditional antibiotics and usage strategies, there has been an increased interest in targeted antimicrobials. Ideally, these systems are effective only against a single microorganism or one small group of microorganisms, are is difficult for microbes to develop a resistance, are nontoxic to humans, maintained in the system long enough to be effective, and easily secreted one the desired effect has been achieved.

1.2 Metallic Nanoparticles

Innovations in the manipulation, and understanding of inorganic nanoparticles and their characteristics has allowed for investigations into their use in a variety of biomedical applications as antimicrobials, contrast agents, drug delivery vehicles, and diagnosis aids. Particularly, control over size, shape, and surface chemistry have allowed for their tunability to a number of situations [2, 3]. Size is especially tunable and can greatly influence how particles behave *in vivo*. Nanoparticles under 100 nm can pass through the blood-brain barrier and those under 200 nm have increased uptake by cells [4]. Nanoparticles small size also offers a greatly increased surface area to volume ratio and can therefore hold a greater payload on their surface per unit mass than a bulk materials [3]. Metallic nanoparticles can also offer greater stability to molecules attached to them while *in vivo* [3]. However, nanoparticles made of some material have been shown to induce acute toxicity, and this must be tested for with any biomedical nanoparticle system [4].

Size & characteristics

1.2.1 Iron Nanoparticles

Superparamagnetic iron oxide nanoparticles (SPIOINs) are used clinically as a T2 contrast agent for magnetic resonance imaging (MRI) [5]. These particles are made by reducing ionic iron in solution to from particles between 30 and 150 nm [6]. To be considered paramagnetic, a material must produce a magnetic moment only in the presence of a magnetic field, such as the one produced during MRI [7]. SPIONs can be used as a contrast agent in soft tissues which do not inherently provide clear images, such as the liver, spleen, and kidneys [5].

1.2.2 Silver Nanoparticles

Silver impacts microbial systems through several mechanisms resulting in the disruption of many crucial cell functions such as cell wall and nucleic acid synthesis, peptide translation, protein structure, and membrane ion pumps. Because of its multiple modes of action, silver is not only an effective antimicrobial, but also one to which bacteria have difficulty developing a resistance. With these antimicrobial qualities in mind, silver is being utilized in a number of clinical applications including burn wound wrappings, catheters, and dental resins [8]. Additionally, studies in rats have shown that low concentrations of silver in the blood stream do not significantly alter metabolism or cause damage to the liver or blood cells [9].

Silver can be reduced into nanoparticles whose size, morphology, and surface chemistry can be easily controlled and because of its stable noble metal qualities can also be applied in combination with nanoparticles made from other elements [2]. While its ions can be harmful to host cells as well as bacteria, studies have shown that not all forms of silver nanoparticles have cytotoxic effects on mammalian cells in culture [9]. Studies have shown that silver retains its antimicrobial properties even when part of a combination of materials [8]. When used in conjunction with iron, it creates a platform that is both magnetically sensitive and antimicrobial.

1.3 Ligands

Numerous ligands can readily be attached to nanoparticles via chemical bonds, and these ligand experience lessened degradation *in vivo* while attached to nanoparticles. Bonded ligands have a significant impact on the conjugated nanoparticles in terms of solubility, retention *in vivo*, agglomeration, toxicity, and chemical characteristics. The charge of a ligand is an especially important consideration when predicting the qualities

the conjugated ligand will infer. Ligands with charged groups are more likely to contribute to solubility of the particles, while those that are hydrophobic are more likely to intercalate into the cell membrane [10].

Hydroxypropyl cellulose (HPC) and poly(acrylic acid) (PAA) are two ligands incorporated in the conjugate nanoparticles described herein. Both polymers are commonly used to aid in nanomaterial dispersion; they are hydrophilic, negatively charged, nontoxic, and inexpensive. The LD50 of HPC and PAA for mice are >5g/kg and 4.6 g/kg respectively [11, 12].

There are also a number of ligands which can lend their antimicrobial properties to nanoparticle conjugates. Antimicrobial peptides are naturally produced by many organisms to combat infections and have shown some promise as an antimicrobial [13]. However because of their high cost of production and their high rate of degradation from proteases outside of their host organism, new molecules with antimicrobial properties are being explored. One group, called ceragenins or cationic steroidal antimicrobials, have been shown to be effective against a number of drug-resistant bacteria such as, *P. aeruginosa* [14], *H. pylori* [15], and *S. aureus* [16]. CSA-124 was synthesized by adding a thiol group onto an existing ceragenin, CSA-13, in order to allow for conjugation via a thiol linkage.

1.4 Docosahexaenoic Acid (DHA)

Polyunsaturated fatty acids are an essential dietary nutrient. A particular type of variety of these fatty acids, omega-3 polyunsaturated fatty acids, plays a large role at the cellular level. They interact the cell membrane causing it to be more fluid, flexible, permeable, thus affecting the activity of membrane bound enzymes [17]. Additionally,

they can act as buffers for oxidative stress on cells under stressful conditions [18]. Clinical data suggest that omega 3's reduce the chances of developing heart disease, cancer, and arthritis as well as improve cognitive function [19] and reduce inflammation [20]. One omega-3, docosahexaenoic acid (DHA), has been implicated in increasing the rate of recovery in a variety of injuries related to the nervous system [21-23]. Creating nanoparticle of omega 3 fatty acids with increased surface area may increase the bioavailability of DHA and thus increase its effectiveness as a therapeutic agent [24].

1.5 Organic Nanoparticles

A number of food-grade polymers have been successfully used to encapsulate fatty acids. Plant starches [25, 26], phospholipids [27], and proteins [28, 29]. Three common forms these particles can take are polymeric meshes [25], micelles [29], solid lipid nanoparticles [30], as well as others. Methods commonly used to nanoencapsultate omega-3 fatty acids are homogenization [25], sonication, and spray drying [31]. The principle behind all of these is to create nano-sized globules at an organic-aqueous interface. Surfactants, such as those listed above, accumulate on the surface of the globules via their nonpolar ends, and will either be extracted into the aqueous phase or precipitate out of solution. They then can then be collected by spray drying, lyophilization, or other drying methods.

One polymer that has been used successfully in making organic nanoparticles with a hydrophobic payload is zein [28]. Zein is a well-characterized and widely used protein made by corn plants. It is low-cost, biocompatible, and widely used in a variety of industries such as food processing, pharmaceuticals, and plastics [32]. The amphiphilic nature of zein allows it to interact with hydrophobic substances and solubilize them in

aqueous solutions [28]. This along with its wide usage and well-known characteristics make it an excellent candidate for stabilizing DHA nano-emulsions.

1.6 References

1. Kyne, L., et al., *Health care costs and mortality associated with nosocomial diarrhea due to Clostridium difficile.* Clinical Infectious Diseases, 2002. 34(3): p. 346-353.
2. Pal, S., Y.K. Tak, and J.M. Song, *Does the antibacterial activity of silver nanoparticles depend on the shape of the nanoparticle? A study of the gram-negative bacterium Escherichia coli.* Applied and environmental microbiology, 2007. 73(6): p. 1712-1720.
3. Singh, R. and J.W. Lillard, *Nanoparticle-based targeted drug delivery.* Experimental and molecular pathology, 2009. 86(3): p. 215-223.
4. Qureshi, A.T., et al., *Antimicrobial biocompatible bioscaffolds for orthopaedic implants.* Journal of tissue engineering and regenerative medicine, 2014. 8(5): p. 386-395.
5. Schweiger, C., et al., *MRI contrast enhancement potential of different superparamagnetic iron oxide nanoparticle (SPION) formulations.* Journal of Controlled Release, 2010. 148(1): p. e67-e68.
6. Babes, L., et al., *Synthesis of iron oxide nanoparticles used as MRI contrast agents: a parametric study.* Journal of Colloid and Interface Science, 1999. 212(2): p. 474-482.
7. Na, H.B., I.C. Song, and T. Hyeon, *Inorganic nanoparticles for MRI contrast agents.* Advanced Materials, 2009. 21(21): p. 2133-2148.
8. Monteiro, D.R., et al., *The growing importance of materials that prevent microbial adhesion: antimicrobial effect of medical devices containing silver.* International journal of antimicrobial agents, 2009. 34(2): p. 103-110.
9. Kim, Y.S., et al., *Twenty-eight-day oral toxicity, genotoxicity, and gender-related tissue distribution of silver nanoparticles in Sprague-Dawley rats.* Inhalation toxicology, 2008. 20(6): p. 575-583.
10. Davis, M.E. and D.M. Shin, *Nanoparticle therapeutics: an emerging treatment modality for cancer.* Nature reviews Drug discovery, 2008. 7(9): p. 771-782.
11. Williams, R., *Hydroxypropyl Cellulose.* Material Safety Data Sheet.
12. Sigma-Aldrich, *poly(acrylic acid).* Material Safety Data Sheet, 2006.
13. Zasloff, M., *Antimicrobial peptides of multicellular organisms.* Nature, 2002. 415(6870): p. 389-395.
14. Chin, J.N., et al., *Potential synergy activity of the novel ceragenin, CSA-13, against clinical isolates of Pseudomonas aeruginosa, including multidrug-resistant P. aeruginosa.* Journal of antimicrobial chemotherapy, 2008. 61(2): p. 365-370.
15. Leszczyńska, K., et al., *Bactericidal activities of the cationic steroid CSA-13 and the cathelicidin peptide LL-37 against Helicobacter pylori in simulated gastric juice.* BMC microbiology, 2009. 9(1): p. 187.

16. Chin, J.N., et al., *Antimicrobial activities of ceragenins against clinical isolates of resistant Staphylococcus aureus.* Antimicrobial agents and chemotherapy, 2007. 51(4): p. 1268-1273.
17. Higdon J, D.V., Jump DB, *Essential Fatty Acids.* Linus Pauling Institute Micronutrient Information Center, 2009.
18. Milne, G.L., J.D. Morrow, and M.J. Picklo, *Elevated oxidation of docosahexaenoic acid, 22: 6 (n− 3), in brain regions of rats undergoing ethanol withdrawal.* Neuroscience letters, 2006. 405(3): p. 172-174.
19. Fenton, W.S., et al., *A placebo-controlled trial of omega-3 fatty acid (ethyl eicosapentaenoic acid) supplementation for residual symptoms and cognitive impairment in schizophrenia.* American Journal of Psychiatry, 2001. 158(12): p. 2071-2074.
20. Kelley, D.S., et al., *DHA supplementation decreases serum C-reactive protein and other markers of inflammation in hypertriglyceridemic men.* The Journal of nutrition, 2009. 139(3): p. 495-501.
21. Hong, S.-H., et al., *Docosahexaenoic acid improves behavior and attenuates blood–brain barrier injury induced by focal cerebral ischemia in rats.* Experimental & translational stroke medicine, 2015. 7(1): p. 3.
22. Musto, A.E., et al., *Hippocampal Neuro-Networks and Dendritic Spine Perturbations in Epileptogenesis Are Attenuated by Neuroprotectin D1.* PloS one, 2015. 10(1).
23. Rice, D.S., et al., *Adiponectin receptor 1 conserves docosahexaenoic acid and promotes photoreceptor cell survival.* Nature communications, 2015. 6.
24. Acosta, E., *Bioavailability of nanoparticles in nutrient and nutraceutical delivery.* Current Opinion in Colloid & Interface Science, 2009. 14(1): p. 3-15.
25. Lesmes, U., J. Barchechath, and E. Shimoni, *Continuous dual feed homogenization for the production of starch inclusion complexes for controlled release of nutrients.* Innovative Food Science & Emerging Technologies, 2008. 9(4): p. 507-515.
26. Zeng, D., et al., *One-step synthesis of amphiphilic hyperbranched amylopectin derivatives, characterization and use as functional nanovehicles.* Carbohydrate polymers, 2013. 98(1): p. 905-913.
27. Cui, F., et al., *Biodegradable nanoparticles loaded with insulin–phospholipid complex for oral delivery: preparation, in vitro characterization and in vivo evaluation.* Journal of controlled release, 2006. 114(2): p. 242-250.
28. Luo, Y., Z. Teng, and Q. Wang, *Development of zein nanoparticles coated with carboxymethyl chitosan for encapsulation and controlled release of vitamin D3.* Journal of agricultural and food chemistry, 2012. 60(3): p. 836-843.
29. Zimet, P., D. Rosenberg, and Y.D. Livney, *Re-assembled casein micelles and casein nanoparticles as nano-vehicles for ω-3 polyunsaturated fatty acids.* Food Hydrocolloids, 2011. 25(5): p. 1270-1276.
30. Mehnert, W. and K. Mäder, *Solid lipid nanoparticles: production, characterization and applications.* Advanced drug delivery reviews, 2001. 47(2): p. 165-196.
31. Jafari, S.M., et al., *Nano-particle encapsulation of fish oil by spray drying.* Food Research International, 2008. 41(2): p. 172-183.

32. Shukla, R. and M. Cheryan, *Zein: the industrial protein from corn.* Industrial Crops and Products, 2001. 13(3): p. 171-192.

CHAPTER 2. DIAGNOSTIC ANTIMICROBIAL NANOPARTICLES

2.1 Summary

New synthesis techniques are providing increasing control over many inorganic nanoparticle characteristics, facilitating the creation of new multifunctional theranostics. This report proposes the synthesis and testing of a combination nanoparticle comprised of a maghemite core for enhanced T2 MRI contrast diagnostics, a colloidal silver shell acting as an antimicrobial and therapeutic vehicle, and a ceragenin (CSA-124) surfactant providing microbial adhesion. A poly(acrylic acid) functionalized maghemite nanoparticle is synthesized by a high temperature organic phase reduction followed by thiol functionalization and gold cluster seeding. A silver shell is formed through $AgNO_3$ reduction, and an oriented monolayer of the thiolated ceragenin, is bound through a self-assembly process. The process and products are characterized throughout synthesis through TEM, DLS, FT-IR, UV–Vis, ICP-OES, HPLC-ESI-TOF-MS, DC magnetization and susceptibility, X-ray diffraction, and *in vitro* MRI. Synthesized Diagnostic Antimicrobial Nanoparticles (DANs) were found to have a spherical morphology with a diameter of 32.47 ± 1.83 nm, hydrodynamic diameter of 53.05 ± 1.20 nm, maximum magnetic moment of 12 emu/g NP (54 emu/g Fe) with little variation due to temperature, and are predominantly paramagnetic. *In vitro* MRI studies show that DANs contrast well at concentrations as low as 9 ppm, and successfully adhere to *Staphylococcus aureus.* DAN MIC was determined to be approximately 12 ppm and 24 ppm against *S. aureus and Escherichia coli* respectively.

2.2 Materials and Methods

2.2.1 Materials

The following materials were ordered from Sigma–Aldrich®: poly(acrylic acid) (average MW 1800), triethylene glycol (99%), iron acetylacetonate (99.9%), ethyl-dimethyl-aminopropylcarbodiimide, cysteamine hydrochloride (⩾98%), 2-(N-morpholino)ethanesulfonic acid, silver nitrate (>99%), ammonium hydroxide (28–30%), N-hydroxysulfosuccinimide (98.5%), sodium hydroxide (NaOH), tetrakis(hydroxymethyl)phosphonium chloride (THPC, 80% in water), tetrachloroaurate trihydrate ($HAuCl_4$), and dialysis membranes (10,000 Da). Acetic acid (99%) was obtained from Fisher Scientific®. Formaldehyde (36.5–38%) was obtained from Mallinckrodt Chemicals®. CSA-124 was prepared by functionalizing a ceragenin, CSA-13, with a thiol group on a short PEG tether. Synthetic details for CSA-124 will be reported elsewhere. All other chemicals were used as received unless otherwise noted. Mueller Hinton Broth, and Nutrient Agar, pH6.0 with 0.8%NaCl was purchased from Himedia®/VWR™.

2.2.2 DANs Synthesis

2.2.2a Poly(acrylic acid)-Coated Iron Nanoparticle Synthesis

Iron-poly(acrylic acid) nanoparticle (Fe–PAA NP) synthesis was based on the thermal decomposition methods employed by Ling et al. [1]. All reactions were conducted in an argon atmosphere. First, 1.0 g of poly(acrylic acid) was added to 25 mL triethylene glycol, followed by the addition of 2.0 mM (706 mg) iron acetylacetonate ($Fe(acac)_3$) solution and stirred until dissolved. Using a Glas-Col 500 mL, 325 W heating mantle regulated by a Glas-Col power regulator the mixture was slowly heated to 190 °C over

30 min, then rapidly heated to reflux at 275 °C where the temperature was held for 20, 30, or 40 min.

To purify the resulting mixture, 30 mL ethyl acetate (EtOAc) was added. The mixture was shaken and then centrifuged at 5870*g* for 30 min. The supernatant (EtOAc and dissolved impurities) was removed and discarded. The black precipitate was further purified via liquid/liquid extraction by first re-suspending in 5–10 mL DI water and then adding 20–30 mL EtOAc, centrifuging once at 3000 g for 5 min, and removing the supernatant of EtOAc and dissolved impurities. The liquid/liquid extraction process was repeated for a total of two iterations. Removal of residual EtOAc was accomplished via dialysis (MW cutoff 10,000 Daltons) over a 24–36 h period. This procedure yielded a solution of 28.5 ppm iron content. The Fe–PAA NPs were characterized using TEM, DLS, ICP-OES, and FT-IR.

2.2.2b Thiol Functionalization

For each 1 mL of Fe–PAA NP used, 0.4 mL 2-(N-morpholino)ethanesulfonic acid (MES buffer) at 500 mM and 2.6 mL DI water were added and mixed. Next, 3.5 mL EDC/sulfo-NHS solution (52 mM EDC & 10.13 mM Sulfo-NHS) was added to the solution and allowed to react at 37 °C and under gentle agitation for 30 min. To this solution, 0.5 mL cysteamine hydrochloride at 0.265 mM was added and left to react at room temperature for 4 h. Purification was conducted by 24-h dialysis, during which time the water bath was exchanged three times. This procedure yielded an 8.0 mL solution of 2.75 ppm iron content.

2.2.2c Gold Nanoparticle Synthesis

Gold NPs with approximate diameters of 3.9 ± 0.1 nm were prepared using a modification of the procedure outlined by Duff et al. Briefly, 1.0 mL of 0.06 mmol NaOH and 2 mL of THPC (12 μL in 1 mL of DI water) were mixed with 200 mL of DI water. After 15 min, 4 mL of 1% (w/v) aqueous $HAuCl_4$ was added and continued to stir for an additional 40 min. The solution immediately transitioned from clear to a red–yellow colored solution. Before use, the gold NPs were refrigerated and aged for 3 days.

2.2.2d Gold Seeding

A 3 mL aliquot of gold NP solution (18.7 ppm) was mixed with the 8 mL thiol-functionalized MNP solution for 3 h at 25 °C. The sample was then centrifuged at 9180*g* for 10 min. Centrifugation was repeated for a total of three times, removing the supernatant between each iteration. After completion of the third centrifugation, the pellet was resuspended in 2.5 mL DI water, resulting in a solution of 0.300 ppm iron content. The concentrations of gold seeded iron nanoparticles (Au–Fe–PAA) were measured using ICP-OES and images were obtained using TEM (specific protocols below).

2.2.2e Silver Shell Formation

Silver shell formation was conducted according to a modification of the method of the Jackson and Halas [2]. Silver was reduced on the gold seeded, iron core as follows: 2.0 mL of 5 mM $AgNO_3$ was added to the 2.5 mL Au–Fe–PAA NP solution and mixed. Seventy micro liters of formaldehyde solution (36.5–38%) was then added and mixed. Finally, 20 μL ammonium hydroxide (28–30% NH_3 content) was added in 5 μL increments, stirring between additions. Formaldehyde is the reducing agent and ammonium hydroxide is added to elevate the pH thus driving the formaldehyde/silver

nitrate reaction forward. After the addition of ammonium hydroxide, a visible change in color from translucent purple-brown to dark brown-black was observable with the unaided eye. This procedure yielded a 4.6 mL solution of 60.5 ppm iron content.

2.2.2f CSA Self-Assembly

Immediately after completion of the silver coating process, 50 μL of 0.17 mM CSA solution (CSA, DI water, and acetic acid at a pH 4.5) was added and mixed for 1 h. The resulting nanoparticle solution was purified via dialysis as described above.

2.2.3 Fourier Transform Infrared Spectroscopy (FT-IR)

FT-IR measurements and analysis were performed on freeze-dried samples of Fe–PAA nanoparticles and cysteamine functionalized Fe–PAA NP using a Bruker Tensor 27 FT-IR using a standard room-temperature DTGS detector & OPUS 6.5 Data Collection Program. The freeze-dried samples were ground onto the surface of a KBR plate and measured. The absorbance values were normalized against a KBR plate with no sample.

2.2.4 Ultraviolet-visible Spectroscopy

The UV–Vis results were obtained using a ThermoSpectronic Genesys 6 (Rochester, NY) using Malvern ZEN0040 disposable cuvettes. Nanoparticle samples were diluted to roughly 0.02 ppm in DI water and filtered using a Thermo Scientific Nalgene 0.2 μm surfactant-free cellulose acetate membrane. Absorbance was recorded from 200 to 700 nm at 25 °C.

2.2.5 X-ray Diffraction

The core–shell nanoparticles were characterized by powder X-ray diffraction to determine the structure of the iron oxide core. Diffraction experiments were performed

using a Bruker Kappa APEX II CCD single crystal diffractometer equipped with a Mo Kα source (λ = 0.71073 Å) and graphite monochromator. Approximately 0.1 mg of core–shell nanoparticles was adhered to the tip of a MiTeGen fiber using Paratone-N oil. A series of five phi scans (image width = 180°) were then collected with different detector orientations covering a 2θrange of 10–50° at a detector distance of 100 mm. These images were merged and integrated using the XRD^{2}Eval program in the Bruker APEX2 software. A background subtraction was applied using the EVA 2 program.

2.2.6 Dynamic Light Scattering (DLS)

Hydrodynamic diameters were measured using a Malvern Zetasizer nano series (Worcestershire, UK). NP samples from various stages of synthesis were diluted to roughly 0.02 ppm in $NaHCO_3$/DI (100 mM) then filtered using a Thermo Scientific Nalgene 0.2 μm surfactant-free cellulose acetate membrane. Samples were measured in Malvern ZEN0040 disposable cuvettes at 25 °C.

2.2.7 Transmission Electron Microscopy (TEM)

The TEM images were obtained using a JOEL 2011 TM (Tokyo, Japan). Nanoparticle samples were diluted to roughly 20 ppm in DI water, sonicated for 5 min, and 5 μL was applied to an Electron Microscopy Sciences carbon film 400 square mesh copper grid and allowed to air dry. Images were taken at 150,000×. TEM images were analyzed using Metamorph Advanced software. The diameters of 25 nanoparticles of each type were measured using digital calipers and statistical significance was determined using a one sample *t*-test.

2.2.9 High Performance Liquid Chromatography-Electrospray Ionization Tandem Time of Flight Mass Spectrometry (HPLC-ESI-TOF-MS)

A five point standard curve, $R^2 = 0.9942$, was constructed by comparing known concentrations of CSA-124 dissolved in 25% v/v acetonitrile (ACN) in DI to the integrated area of its HPLC-ESI-TOF-MS peak. CSA-124 displaced from DANs and run through HPLC-ESI-MS/MS were then quantified by comparison to this standard curve. To remove CSA from the DAN, 5.5 μL DL-Dithiothreitol (DTT) was added to 500 μL DANs and allowed to react for 1 h at 37° C. The DTT displaces the CSA from the DANs surface resulting in DTT-DANs and a solution of CSA and unreacted DTT. This was then separated via centrifugation for 15 min at 12*g*. The supernatant was removed and concentrated from 500 μL to 250 μL by vacufugation and 250 μL of ACN/DI (50% v/v) was then added to the solution bringing the final solution to 25% ACN. The samples were then analyzed by HPLC-ESI-TOF-MS (Agilent 1200 with a binary pump/Agilent ESI TOF 6210 PALO ALTO, CA). The LC column used was a normal phase Acclaim® Mixed-Mode HILIC-1, 3 μm Analytical (2.1 × 150 mm). Samples and standards were injected at 2 μL. The first mobile phase was 90% ACN in water with 0.1% formic acid while the second mobile phase was water with 0.1% formic acid. The ESI parameters used are as follows: nitrogen temperature 325 °C, nitrogen flow 5 L/min, nebulizer pressure 20 psi. The DTT-DANs pellet obtained from the previously mentioned centrifugation was quantified by ICP-OES.

2.2.10 DC Magnetization and Susceptibility

The magnetic properties of the nanoparticles were measured with a Quantum Design Physical Property Measurement System (PPMS) using the ACMS option. This utilizes a DC, Faraday-extraction technique in which the sample is quickly pulled (at a

speed of 100 cm/s) through a set of detection coils. Zero-field cooled (ZFC) and field-cooled (FC) magnetic susceptibility data were measured as a function of temperature at a constant field of 1000 Oe. The magnetic hysteresis of the nanoparticles was determined from the field dependence of the DC magnetization from 0 to ±9 T at a temperature of 3 K.

2.2.11 Contrast Concentration Dependence

To determine contrast dependence on DAN concentration, five 1.5 mL centrifuge tubes were filled with an agarose/DAN solution and imaged with MRI at the following concentrations: o ppm, 1.6 ppm, 3.3 ppm, 9.8 ppm, and 27.9 ppm. Also, to determine the impact the DAN's silver shell has on its contrast capabilities, five 1.5 mL centrifuge tubes were filled with a solution of agarose and the iron oxide core at the following concentrations: 0.0 ppm, 1.6 ppm, 3.3 ppm, 9.6 ppm, and 26.6 ppm. These ten samples were aligned and imaged in a single image using the following parameters: TR: 3000, TE: min/full, EC: 1/1 41.7 kHz, FOV: 16 × 12/z, thickness 6 mm. The resulting image was analyzed using image J and the gray scale values of each sample were recorded.

2.2.12 Magnetic Resonance Imaging (MRI)

Sample preparation for magnetic resonance imaging (MRI) was conducted as follows. 10 mL of Muller Hinton Broth (MBH) was inoculated with one loop of *S. aureus* and incubated 24 h at 37 °C. Three mL of inoculated broth was then added to two test tubes. To one of these test tubes 300 μL DANs at 200 ppm was added, while the other test tube received 300 μL Ag–Au–Fe–MNP (no CSA) at 200 ppm. Two other test tubes were prepared by adding 3 mL DI and 300 μL DANs. These four solutions were allowed to rest at room temperature for 30 min, then all were filtered through a 0.45 μm,

surfactant-free, cellulose acetate syringe filter with the exception of one of the DAN/DI samples which serves as a positive control and was filtered using a 0.2 μm filter. The filters were removed from their casing and suspended in the center of at block of agarose approximately 2″ × 3″ × 3″ in size. All samples were imaged under the following parameters: TR: 3000, TE: min/full, EC: 1/1 41.7 kHz, FOV: 16 × 12/z, thickness 1 mm.

2.2.13 Minimum Inhibitory Concentration (MIC)

The minimum inhibitory concentration (MIC) was determined using a protocol modified from that of Andrews [3]. Briefly, the inoculum was prepared by mixing one loop of the desired bacteria in 10 mL of Mueller Hinton Broth (MHB), which was then incubated at 37 °C overnight. This inoculum was found to be 1.6×10^8 cfu/mL by plating serial dilutions. For testing, inoculum was used promptly that day and diluted to 1×10^6 cfu/mL. In preparation of the serially diluted 96 well plate, 100 μL of pure MHB was added to each well. Next 100 μL of the DANs solution, at 96.7 ppm, was added to the first well of each row. Then using a multichannel pipette set to 100 μL, the DANs/MHB solution was serially diluted across, thus making each consecutive well 50% the concentration of the well preceding it. At this time 100 μL of the prepared inoculum was added to each well and the plate was incubated overnight. The MIC is defined as the most dilute concentration of an antimicrobial that will inhibit visible growth of a microbe after overnight incubation [3]. Each row should contain a live control/negative control, i.e. a well that contains no antimicrobial. Each row should also include a well consisting of only the pure MHB.

2.3 Results and Discussion

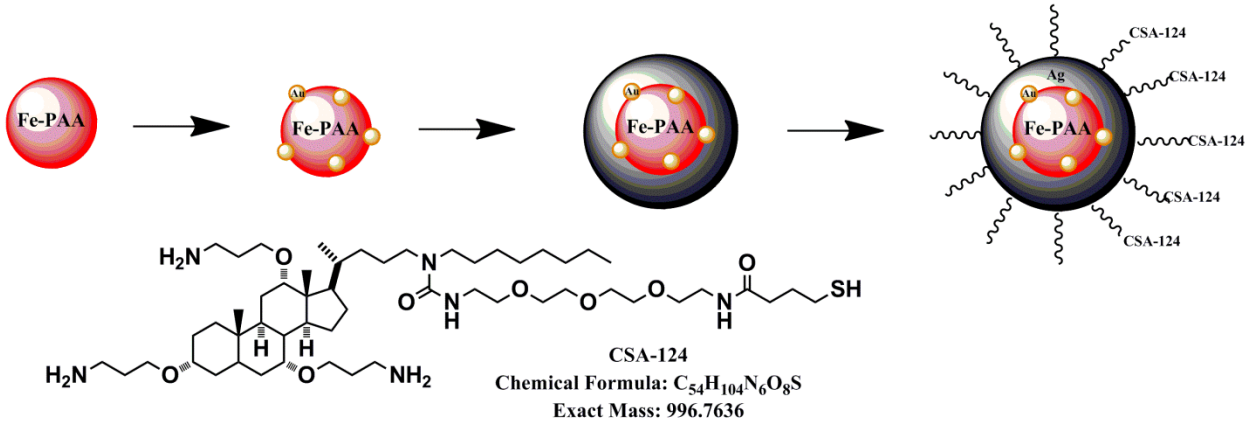

Figure 2.1. An overview of the synthesis process is presented. Fe–PAA NPs are synthesized; they are then functionalized and seeded with gold NPs (1). Silver ions from $AgNO_3$are reduced onto the gold particles (2). Finally, CSA-124 is bound to the surface of the silver shell (3).

The DANs synthesis is a multi-step procedure and is outlined in Figure 2.1. The core of the DAN is an iron nanoparticle with a polyacrylic surface ligand (Fe–PAA) synthesized through thermal reduction of iron oxide in an organic solvent. After synthesis, the poly(acrylic acid) surfactant is modified with cysteamine through an ethyl-dimethyl-aminopropylcarbodiimide (EDC) chemistry reaction (described in Figure 2.2), resulting in a distal thiol group on the poly(acrylic acid) that will readily bind with gold and silver. The cysteamine "activated" product is then reacted with gold nanoparticles, or "seeds", which interact with functionalized Fe–PAA through thiol linkages [4]. This seeded surface provides nucleation sites for silver reduction and shell formation resulting in a colloidal shell several nanometers thick. Lastly, the CSA-124 is attached to the silver shell via its thiolated ethylene glycol side chain providing a uniform orientation of the compound with two primary amines on the distal portion of the molecule free to interact with the environment.

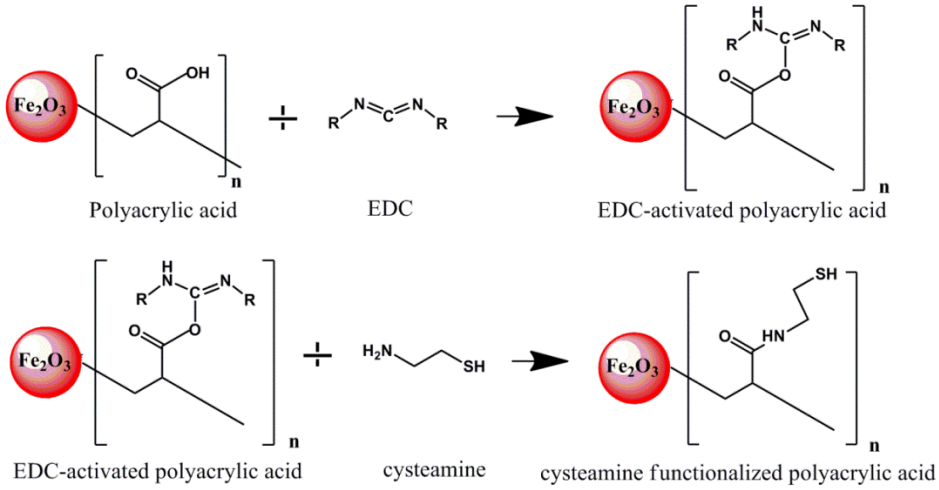

Figure 2.2. Functionalization schematic of the PAA surfactant through an EDC/Sulfo-NHS workup. Carboxylic acids are activated with EDC then functionalized with cysteamine, resulting in terminal thiols allowing for strong gold seed adhesion.

Functionalization of the iron with poly(acrylic acid) provides for a hydrophilic particle improving colloidal solubility in the follow-on aqueous reactions. Additionally the PAA surfactant provides a platform for gold seeding and colloidal shell formation. The functionalization procedure of PAA was modified from of the protocol Ken-Tye Yong et al. developed for the functionalization of carboxylate modified polystyrene beads [5]. The carboxyl groups of the PAA were activated by ethyl-dimethyl-aminopropylcarbodiimide (EDC) and N-hydroxysulfosuccinimide (Sulfo-NHS), and then reacted with the primary amine groups of cysteamine hydrochloride (CH), resulting in an amide bond linkage. An EDC/Sulfo-NHS workup is a well-established, facile method for bonding molecules through their carboxylic and amine groups and has also been utilized in CA/BMPA-coating magnetic nanoparticles [6], protein coupling [7], and protein film deposition [8]. Once bound to the NP surface, the cysteamine offered a primary thiol group that was ideal for the attachment of colloidal gold used in shell growth.

The method of colloidal attachment of gold nanoparticles to the thiol-functionalized PAA and silver reduction was based on a method previously presented by Jackson and Halas [2]. In our modification, silver from $AgNO_3$ was reduced onto the gold seed nucleation sites bound to the PAA through cysteamine. This method provides adequate control over shell thickness while maintaining colloidal stability in follow-on aqueous CSA functionalization reactions. The CSA functionalization reaction is conducted immediately following silver shell reduction to add bulky surface groups providing steric hindrance and bound surface charges to reduce agglomeration of the finished particles. If surface functionalization is not conducted within hours of the silver reduction step, particles will rapidly agglomerate.

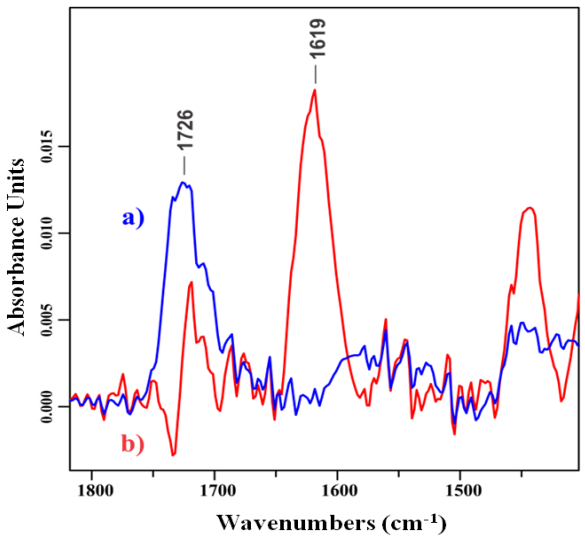

Figure 2.3. The FT-IR spectra shown indicate a shift in bond energy of (a) unmodified Fe-PAA upon (b) functionalization with cysteamine.

The composition of the nanoparticles was analyzed using FT-IR, ICP-OES, and UV–Vis. FT-IR was employed to verify the addition of cysteamine to the carboxyl-terminus of the poly(acrylic acid) surfactant on the Fe–PAA NP. In this reaction, a carboxyl group is converted into an amide bond (as seen in Figure 2.3). The FT-IR peaks

for carboxyl and amide groups are commonly found at 1780–1710 cm^{-1} and 1690–1620 cm^{-1}, respectively [9]. In the FT-IR spectra of Fe–PAA NPs in Figure 2.3a there is a clear peak at 1726 cm^{-1} indicative of the carboxyl group. In Figure 2.3b the 1726 cm^{-1} maxima peak is greatly reduced while a clear peak arises with a 1619 cm^{-1} maxima indicating that many, though not all, of the carboxyl groups have been converted to amides.

Through ICP-OES, concentrations of iron, gold, and silver were monitored throughout the synthesis process. Using this information and the known sample volumes it was possible to track the mass balance of each element. ICP-OES data shows that the compositions of DANs are 76.64% silver, 22.75% iron, and 0.61% gold. Based on the mass balance of iron, it was determined that the synthesis procedure from Fe–PAA NPs through functionalization, gold seeding, and silver coating resulted in a 8.6% yield with the bulk of losses being attributed to centrifugal purification. It is suspected that substituting magnetic separation for centrifugation during the purification process could minimize these losses. Iron was chosen to be the element monitored for percent yield because it was the only element added in the first step and not introduced again throughout the process.

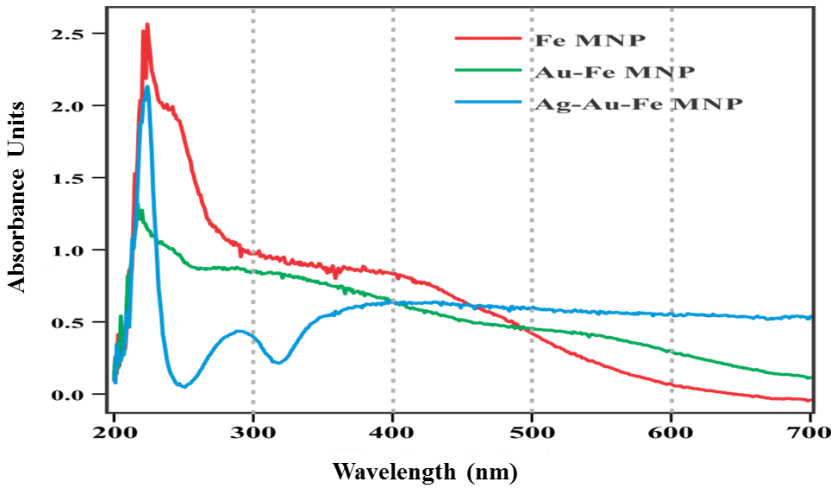

Figure 2.4. UV–Vis absorption spectra of DANs at different stages of development are shown. Series (a) shows Fe–PAA NP, (b) shows Au–Fe–PAA NP, and (c) shows Ag–Fe–PAA.

UV–VIS spectroscopy was used to monitor to process progress between steps. After NP-PAA functionalization, curve "a" in Figure 2.4 was obtained. This curve served as a baseline or comparison point for subsequent measurements. Curve "b" represents the UV–Vis spectra obtained after purification of gold seeded Fe–PAA NPs. This curve clearly differs from the baseline curve and closely parallels the absorbance spectra of a gold NP control.

The similarity between the Au–MNP and gold seed control curves supports the assertion that gold seeds were successfully attached to the PAA coating of the iron NPs. Curve "c" depicts the absorbance spectra obtained after silver was reduced onto the Au–Fe–PAA. As with the gold seeded NPs, the silver coated NP curve is distinctly different from both the previous curves and shows the clear red shifting commonly associated with metal nanoshell synthesis [2]. This strongly indicates that a silver shell was successfully reduced onto the particle surface, thus supporting the ICP-OES findings.

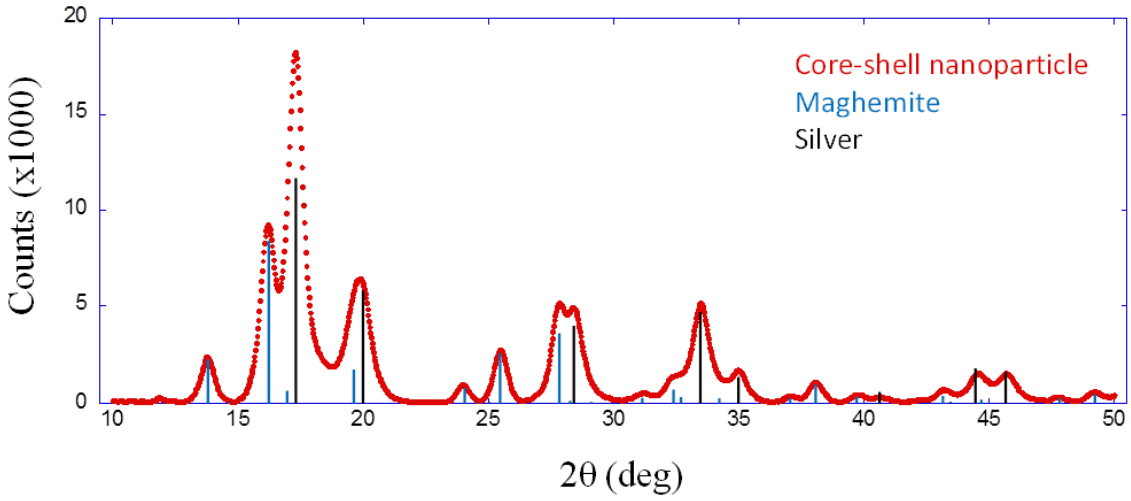

Figure 2.5. X-ray diffraction pattern of DAN core is representative of Silver and Maghemite.

To determine the exact structure of the DAN's iron oxide core, X-ray diffraction was employed. A powder diffraction pattern of the core–shell nanoparticles is shown in Figure 2.5. The reflections due to the iron oxide core are indexed as blue lines and the reflections due to the silver shell are indexed as black lines. The indexed reflections indicate that the iron oxide core is maghemite. This is consistent with the brown color of the core nanoparticles.

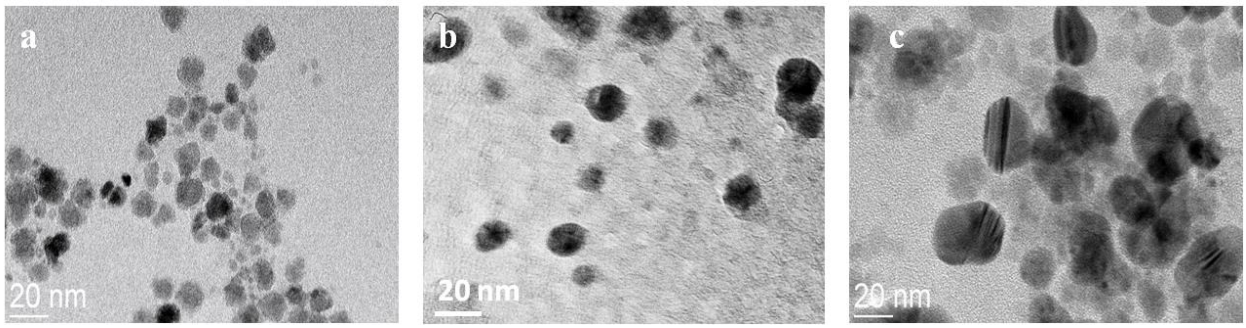

Figure 2.6. TEM images of the nanoparticles at three stages of development are shown: (a) Fe–PAA nanoparticles, (b) Au–Fe–PAA, and (c) Ag–Fe–PAA with CSA-124 surfactant.

The shape and size of nanoparticles at various stages of synthesis were determined using a combination of TEM and DLS. The TEM images displayed in Figure

2.6 shows the growth of the nanoparticles as gold seeds were attached (Figure 2.6b) and a silver shell was reduced onto the Fe–PAA NP (Figure 2.6c). It is also evident that the Fe–PAA NPs have a rough spherical morphology that became more regular and smooth as gold and silver were added in following processes.

Table 2.1. Nanoparticle diameters as determined by TEM.

Table 1: Nanoparticle Diameters as Determined by TEM	
nanoparticle	average diameter (nm)
Fe-PAA NP	9.415 +/- 0.539
Au seeded-Fe-PAA NP	11.086 +/- 0.527
DAN	32.474 +/- 1.830
Hydrodynamic Diameters as Determined by DLS	
nanoparticle	hydrodynamic diameter (nm)
Fe-PAA NP	45.563 +/- 1.047
DAN	53.053 +/- 1.202
*DLS was conducted in 100mM $NaHCO_3$ at 25° C	

Analysis of the TEM images using Advanced Metamorhph was used to determine nanoparticle size and is presented in Table 1. One sample *t*-test analysis of these values found that the diameter increase after gold seeding was not statistically significant ($P > 0.05$) while the diameter increase after silver shell reduction was ($P < 0.05$). Hydrodynamic diameters, as determined through DLS, are also included in Table 1. As expected from a reasonably monodisperse product there is substantial agreement between the values generated from the TEM image and the DLS results. As the multi-step synthesis continues larger particles with larger hydrodynamic diameters are produced as a result of the addition of the silver coating and CSA-124 addition.

To quantify the CSA bound to colloidal silver, a standard curve of integrated peak area vs. CSA concentration was constructed using HPLC-ESI-TOF-MS. CSA was then displaced from the DAN surface and analyzed, again using HPLC-ESI-TOF-MS. The corresponding CSA concentration was determined to be 1.34 mg/L for a 500 μL sample, or 4.01×10^{14} CSA molecules. Using ICP-OES it was determined the same 500 μL sample contained roughly 5.27×10^{12} DANs, thus we conclude there are on average 76.1 CSA-124 molecules bound to each DAN.

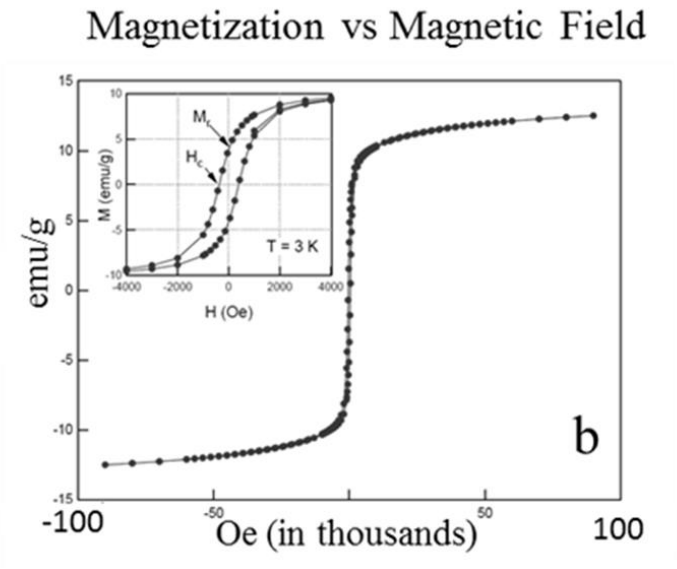

Figure 2.7. The hysteresis loop shows NP magnetization as a function of magnetic field.

Figure 2.7 is a hysteresis loop of the DANs. The DAN magnetization was measured as a function of applied field from 0 to ±90,000 Oe. As seen in the graph, the magnetization of DANs increases quickly with the applied field, tending toward saturation at fields >5000 Oe. The maximum magnetization is roughly 12 emu/g NP, which is 54 emu/g Fe. This value is comparable to the iron oxide T2 contrast agents currently in clinical use; Feridex and Combidex have magnetizations of 45 emu/g Fe and 61 emu/g Fe respectively [10]. DAN magnetic moment was also evaluated with respect to

temperature and found to have a slightly inverse relationship, however still maintained a sufficient magnetic moment at physiological conditions, dropping less than 20% over a 300 K increase.

The inset shows an expanded view of the low-field region of the magnetization in which a hysteresis is observed with a remnant magnetization, $M_r \sim 3.0$ emu/gm, and a coercive field, $H_c \sim 300$ Oe. The data suggest that the majority of the nanoparticles are paramagnetic and at least some subset of the nanoparticles have a ferromagnetic component to their magnetization. This is likely a result of the size distribution of the particles used in the iron core, some of which will be above the critical transition size from superparamagnetic to ferromagnetic, roughly 10 nm [11].

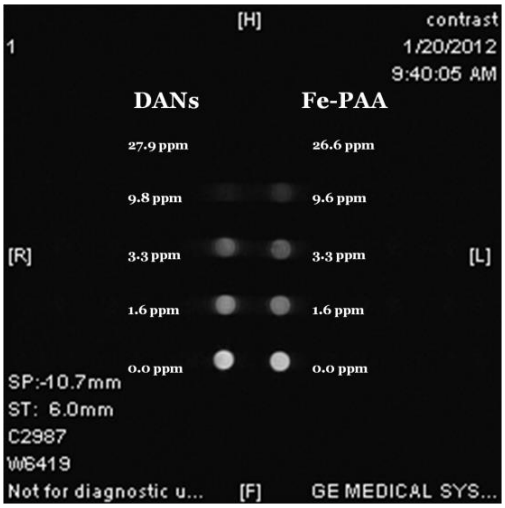

Figure 2.8. MRI of NPs dispersed in agarose at various concentrations (left). Graph of resulting pixel intensity for each sample concentration (right).

In Figure 2.8, a clear correlation is seen between nanoparticle concentration and MRI contrast, known as negative contrast. The paramagnetism of the NP's causes the relaxivity of nearby water molecules to drop, and a decrease in relaxivity results in a lower pixel intensity. Using ImageJ, the pixel intensity of each tube was measured then plotted against particle concentration. On average, pixel intensity drops by 16.7 gray

scale units for each additional ppm DAN. Figure 2.8 also shows the similar contrast of DANs and Fe–PAA NP indicating that the maghemite core is not compromised by the formation of the silver shell. In fact, DANs seem as though they may have slightly increased contrast ability. This can potentially be explained by Dr. Vuong et al. who postulated that surrounding a paramagnetic NP with a shell prevents it from directly coordinating with the select few neighboring water molecules but rather allows its effects to be distributed over a greater surface area and thus affecting a greater number of water molecules. This results in a reduction of the relaxation time of a greater number of water molecules correlating with a greater negative contrast [12].

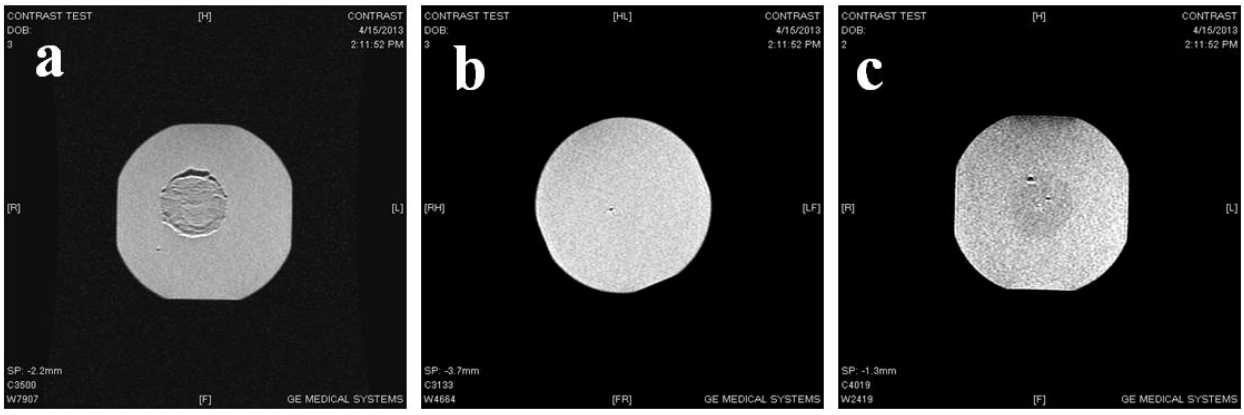

Figure 2.9. Magnetic resonance images of syringe filters suspended in agarose. Image (a) is a positive control, image (b) is a negative control, and image (c) is the treatment.

Determination of *in vitro* contrast of bacteria by DANs was assessed by exposing *S. aureus* to DANs, filtering this solution through a syringe filter, suspending this filter in a block of agarose, and imaging with MRI, seen in image Figure 2.9c. Filter pores, 450 nm, were chosen to be large enough to allow DANs to pass unhindered yet retain all bacteria. As a negative control, *S. aureus* was also exposed to DANs devoid of CSA-124, (Fe core with silver shell only) and filtered, Figure 2.9b. A positive control of total DAN capture using a 200 nm filter that captured bulk of the DAN's on the filter

media can be seen in Figure 2.9a. As anticipated, Figure 2.9a shows the greatest contrast, Figure 2.9b shows no contrast and Figure 2.9c shows moderate contrast. This suggests that DAN attachment does occur, though the efficiency of the attachment is far below 100%. This may be caused by variation in the particle CSA-124 functionalization. As noted above the average functionality is 76.1 CSA/particle but distribution is currently unknown, as such, large numbers of particles may have little or no CSA attached. The images also supports that DANS devoid of CSA do not adhere to the *S. aureus*, nor are they trapped in the filter. To ensure the attachment of CSA-124 to the NP surface did not affect filter permeability, fully conjugated DANs in DI were filtered and also resulted in no contrast (data not shown).

The minimum inhibitory concentration found for DANs suggests they are slightly more effective against *S. aureus* than *E. coli* at 12 ppm and 24 ppm respectively. Ruparelia et al. determined the average MIC of SNPs against four different strains of *E. coli* and three different strains of *S. aureus* [13]. The MIC of SNPs against both *S. aureus* and *E. coli* was found to be 120 ppm. Our own MIC assay using the above protocol with cellulose stabilized-SNP was found to be 250 ppm. This makes DANs approximately ten times more effective against *S. aureus* and five times more effective against *E. coli* according to the results of Ruparelia *et al [13]*.

2.4 Conclusions

The results in this study suggest that the synthesis process described above successfully generates the desired iron containing, silver shell nanoparticle with a ceragenin monolayer surface functionalization. The FT-IR spectrums support the addition of a mercapto group to the Fe–PAA NP. ICP-OES demonstrated the final product is

comprised of 76.64% silver, 22.75% iron, and 0.61% gold with ~8% total yield. Both TEM and DLS results demonstrate predictable growth of the particle with each additive process step. These results indicate that gold and silver were successfully deposited onto the Fe–PAA NPs, yielding a final nanoparticle of 32.474 ± 1.83 nm diameter and 53.053 ± 1.202 nm hydrodynamic diameter. Furthermore, these particles were shown to be predominantly paramagnetic and possess a strong magnetic moment of 54 emu/g Fe. These characteristics are representative of clinically adopted T2 MRI contrast agents, making DANs a good potential candidate for diagnostic use. MRI of DANs and maghemite core NPs at various concentrations suggest a 16.7 gray scale unit reduction in pixel intensity for each ppm DAN. DANs have also demonstrated an ability to adhere and contrast *S. aureus in vitro*. Lastly, DANs have been shown to inhibit *S. aureus* at 12 ppm and *E. coli* at 24 ppm, five times more effective than silver alone. The results presented in the report indicate DANs to be a potentially viable diagnostic contrast agent for treating deep tissue infection. Further work must be done to assess the cytotoxic qualities of DANs as well as their diffusion characteristics using a more advanced tissue phantom.

2.5 References

1. Ling, M.M., K.Y. Wang, and T.-S. Chung, *Highly water-soluble magnetic nanoparticles as novel draw solutes in forward osmosis for water reuse.* Industrial & Engineering Chemistry Research, 2010. **49**(12): p. 5869-5876.
2. Jackson, J. and N. Halas, *Silver nanoshells: variations in morphologies and optical properties.* The Journal of Physical Chemistry B, 2001. **105**(14): p. 2743-2746.
3. Andrews, J.M. and B.W.P.o.S. Testing, *BSAC standardized disc susceptibility testing method.* Journal of Antimicrobial Chemotherapy, 2001. **48**(suppl 1): p. 43-57.
4. Brust, M., et al., *Synthesis of thiol-derivatised gold nanoparticles in a two-phase liquid–liquid system.* J. Chem. Soc., Chem. Commun., 1994(7): p. 801-802.
5. Yong, K.-T., et al., *Synthesis and plasmonic properties of silver and gold nanoshells on polystyrene cores of different size and of gold–silver core–shell*

nanostructures. Colloids and Surfaces A: Physicochemical and Engineering Aspects, 2006. **290**(1): p. 89-105.
6. Lattuada, M. and T.A. Hatton, *Functionalization of monodisperse magnetic nanoparticles.* Langmuir, 2007. **23**(4): p. 2158-2168.
7. Grabarek, Z. and J. Gergely, *Zero-length crosslinking procedure with the use of active esters.* Analytical biochemistry, 1990. **185**(1): p. 131-135.
8. Tengvall, P., et al., *Surface immobilized bisphosphonate improves stainless-steel screw fixation in rats.* Biomaterials, 2004. **25**(11): p. 2133-2138.
9. Merlic, C., *IR Absorption Table*, WebSpectra 2000.
10. Lee, J.E., et al., *Uniform mesoporous dye-doped silica nanoparticles decorated with multiple magnetite nanocrystals for simultaneous enhanced magnetic resonance imaging, fluorescence imaging, and drug delivery.* Journal of the American Chemical Society, 2009. **132**(2): p. 552-557.
11. Dutz, S., et al., *Hysteresis losses of magnetic nanoparticle powders in the single domain size range.* Journal of Magnetism and Magnetic Materials, 2007. **308**(2): p. 305-312.
12. Vuong, Q.L., et al., *A Universal Scaling Law to Predict the Efficiency of Magnetic Nanoparticles as MRI T2-Contrast Agents.* Advanced healthcare materials, 2012. **1**(4): p. 502-512.
13. Ruparelia, J.P., et al., *Strain specificity in antimicrobial activity of silver and copper nanoparticles.* Acta Biomaterialia, 2008. **4**(3): p. 707-716.

CHAPTER 3. CERAGENIN MEDIATED SELECTIVITY OF ANTIMICROBIAL SILVER NANOPARTICLES

3.1 Summary

The understanding that common broad-spectrum antimicrobials disrupt natural microbial flora important in acquiring nutrients and preventing infection has resulted in a paradigm shift favoring more selective antimicrobials. This work explores silver nanoparticles conjugated with ceragenin, or cationic antimicrobials (CSA-SNPs), as a potential Gram-positive selective antimicrobial. Herein, CSA-SNPs are characterized using transmission electron microscopy (TEM), dynamic light scattering (DLS), zeta potential, and high-performance liquid chromatography−electrospray time-of-flight mass spectrometry (HPLC−ESI-TOF-MS). The antimicrobial properties are determined through minimum inhibitory concentration/minimum bactericidal concentration (MIC/MBC) and time-kill studies. Spatial selectivity of the conjugate nanoparticle was evaluated using confocal imaging, MATLAB statistical analysis, and video monitored interactions between bacteria and CSA-SNPs via laser trapping techniques. Cytotoxicity was also determined by live/dead staining and flow cytometry. Average particle size, as determined through TEM analysis, and hydrodynamic diameter, as determined via DLS, are 63.5 ± 38.8 and 102.23 ± 2.3 nm, respectively. The zeta potential of the SNP before and after CSA attachment is −18.23 and −8.34 mV, respectively. MIC/MBC data suggest that CSA-SNPs are 8 times more effective against Staphylococcus aureus than SNPs alone. Furthermore, MATLAB analysis of confocal imaging found that 70% of CSA-SNPs are within 2 μm of *S. aureus*, whereas this percentage falls to below 40% with respect to Escherichia coli. These results are bolstered further by laser trapping

experiments demonstrating selective adherence of CSA-SNPs conjugates with bacterial strains. Cytotoxicity studies of CSA-SNPs against 3T3 fibroblasts indicate 50% cell viability at 50 ppm.

3.2 Materials and Methods

3.2.1 Materials

SmartSilverAS was purchased from NanoHorizons, Inc. (Bellefonte, PA). Dialysis membranes (10 000 Da) were ordered from Sigma-Aldrich. TEM grids and paraformaldehyde (16%) were obtained from Electron Microscopy Sciences (Hatfield, PA). The

Acclaim Mixed-Mode HILIC-1 normal phase LC column was ordered from ThermoScientific (Logan, UT). For cell culture, DMEM-RS, trypsin (0.25%, 1× solution), and DPBS/modified (1×) are HyClone products and are also ordered through ThermoScientific. Sytox Red dead cell stain was purchased from Molecular Probes by Life Technologies Corporation, and a Live BacLight Bacterial Gram Stain Kit was purchased from Invitrogen Molecular Probes (Eugene, OR). CSA-124 was prepared at Brigham Young University by functionalizing an early lead ceragenin, CSA-13, with a thiol group on a short PEG tether. Synthetic details for CSA-124 will be reported elsewhere. All other chemicals were used as received unless otherwise noted. For bacterial culture, Mueller Hinton Broth (MHB) and nutrient agar, pH 6.0 with 0.8% NaCl, were purchased from Himedia/ VWR, and Mannitol Salt Agar was purchased from Acumedia/Neogen Corporation (Lansing, MI).

3.2.2 Conjugating Silver Nanoparticles with CSA-124

A 4 mL suspension of SNPs in deionized (DI) water at 300 ppm was mixed with 50 µL of CSA-124 in DI water at 0.2 mM. This solution was allowed to react overnight at room temperature and was then purified in dialysis sacks, pore size 12 000 Da MWCO, for 24 h. During this time, the water was changed three times.

3.2.3 Dynamic Light Scattering (DLS)

Hydrodynamic diameters were measured using a Malvern Zetasizer nano series (Worcestershire, UK). NP samples from various stages of synthesis were diluted to roughly 0.02 ppm in $NaHCO_3$/DI (100 mM) then filtered using a Thermo Scientific Nalgene 0.2 µm surfactant-free cellulose acetate membrane. Samples were measured in Malvern ZEN0040 disposable cuvettes at 25˚ C. In determination of zeta potential, NPs were suspended in DI, filled a Zetasizer nano series folded capillary cell, and also measured using a Malvern Zetasizer nano series (Worcestershire, UK) at 25˚ C.

3.2.4 Transmission Electron Microscopy (TEM)

The TEM images were obtained using a JOEL 2011 (Tokyo, Japan). Nanoparticle samples were diluted to roughly 25 ppm in DI water and 5 µL was applied to an Electron Microscopy Sciences carbon film 400 square mesh copper grid and allowed to air dry. Images were taken at 150,000X. TEM images were analyzed using Metamorph Advanced software. The diameters of 25 nanoparticles of each type were measured using digital calipers and statistical significance was determined using a one sample t-test.

3.2.5 CSA Quantification

A five point standard curve, $R^2 = 0.9942$, was constructed by comparing known concentrations of CSA-124 dissolved in 25% $^{v}/_{v}$ acetonitrile (ACN) in DI to the integrated area of its HPLC-ESI-TOF-MS peak. CSA-124 was displaced from the SNP and run through HPLC-ESI-MS/MS, then quantified by comparison to this standard curve. To remove CSA from the SNP, 5.5 µL DL-Dithiothreitol (DTT) was added to 500 µL CSA-SNPs and allowed to react for one hour at 37° C. The DTT displaces the CSA from the SNP surface resulting in DTT-SNPs and a solution of CSA and unreacted DTT. Particles were then separated via centrifugation for 15 minutes at 12g. The supernatant was removed and concentrated from 500 µL to 250 µL by vacufugation and 250 µL of ACN/DI (50% v/v) was then added to the solution bringing the final solution to 25% ACN, mirroring the standard curve solution. The samples were then analyzed by HPLC-ESI-TOF-MS (Agilent 1200 with a binary pump/Agilent ESI TOF 6210, Palo Alto, CA). The LC column used was a normal phase Acclaim Mixed-Mode HILIC-1, 3µm Analytical (2.1 x 150mm). Samples and standards were injected at 2 µL. The first mobile phase was 90% ACN in water with 0.1% formic acid while the second mobile phase was water with 0.1% formic acid. The ESI parameters used are as follows: nitrogen temperature 325° C, nitrogen flow 5 L/min, and nebulizer pressure 20 psi. The DTT-SNP pellet obtained from the previously mentioned centrifugation was quantified by ICP-OES.

3.2.6 Cytotoxicity Analysis

Murine 3T3 fibroblast cells were seeded onto 12-well plates in 500 µL of growth medium (DMEM, 10% FBS) and allowed to grow for 48 hours until 80% confluent. The

medium was then replaced with 600 µL of medium containing incremental concentrations of CSA-SNPs. Live controls received 600 µL of the growth medium containing no CSA-SNPs. Dead controls received 600 µL of growth medium as well as 150 µL of 70% ethanol solution. The cells were incubated at 37° C in 5% CO_2.

The 3T3 cells were incubated in the CSA-SNP medium for 24 hours. Then the medium was removed and collected. The cells were lifted from the 12-well plates using Trypsin and collected in combination with the previously removed media. The cells were then separated through centrifugation and resuspended in 1 mL phosphate-buffer saline (PBS; -Ca, -Mg). The cells were stained for viability using Sytox Red, 1 µL for 15 minutes, then separated via centrifugation, and fixed in 350 µL of 1% paraformaldehyde (PFA) solution. The live and dead counts were evaluated using flow cytometry.

3.2.7 Hemolytic Characterization

The hemolytic properties of CSA-SNP were assessed using the ASTM E2524-08 protocol Standard Test Method for Analysis of Hemolytic Properties of Nanoparticles [1]. This test evaluates the effect CSA-SNPs have on the integrity of red blood cells by in vitro exposure and quantification of hemoglobin released. First hemoglobin standards were made covering a range from 0.025 to 0.8 mg/L and a standard curve was generated. Hemoglobin is oxidized to methemoglobin by ferricyanide in the presence of alkali. This concentration can be determined by measuring absorbance at 540 nm. Blood was diluted in PBS ($–Ca^{2+}/Mg^{2+}$), to hemoglobin concentration of 10 mg/mL. In a test tube 700 µL PBS, 100 µL diluted blood solution, and 100 µL CSA-SNP solution were mixed and placed on an orbital shaker for 30 minutes. The samples were then placed in a water bath set to 37 ˚C for 3 hours and 15 minutes. Next samples were centrifuged for 15 minutes at

800x*g* and the supernatant was collected. 100 µL of supernatant was added to a 96 well plate along with 100 µL cyanmethemoglobin reagent, covered, gently shaken, allowed to react for 10 minutes, then its absorbance at 540 nm was measured on a plate reader. This absorbance was compared to the standard curve to determine hemoglobin concentration. This concentration divided by the total hemoglobin concentration of the diluted blood solution yields percent hemolysis. A 10% Triton X solution was used as the positive control to determine total blood hemoglobin. Each sample was run in triplicate and known standards were run with each sample to ensure they matched up properly with the standard curve.

3.2.8 Brightfield Imaging of Cell Morphology

To qualitatively assess cell health after CSA-SNP exposure, 3T3 fibroblasts were seeded with DMEM/10%FBS into 9 wells of a 12 well tissue culture treated plate and incubated at 37˚ C and 5% CO_2 until 50% confluent, about two days. The media was removed from all wells. Three of these wells were exposed to 600 µL DMEM/10%FBS, three received a 600 µL solution of CSA-SNPs in DMEM/10%FBS at 15ppm, and three wells received 600 µL solution of CSA-SNPs in DMEM/10%FBS at 37ppm. Samples were incubated 24 hours, again at 37˚ C and 5% CO_2. Wells were imaged using a Nikon eclipse TS100 Brightfield microscope (Melville, NY), PHOTOMETRICS CoolSNAP camera (Tucson, AZ), and MetaMorph Advanced image analysis software.

3.2.9 Antimicrobial Efficacy

3.2.9a Minimum Inhibitory and Bactericidal Concentrations (MIC/MBC)

The minimum inhibitory concentration (MIC) was determined using a protocol modified from that of J. M. Andrews [2]. Briefly, the inoculum was prepared by mixing one loop

of the desired bacteria in 10 mL of Mueller Hinton Broth (MHB), which was then incubated at 37˚ C overnight. This inoculum was found to be 1.6 x 10^8 cfu/mL by plating serial dilutions. For testing, inoculum was used promptly that day and diluted to 1 x 10^6 cfu/mL. In preparation of the serially diluted 96 well plate, 100 µL of pure MHB was added to each well. Next 100 µL of the antimicrobial solution, CSA-SNPs mixed in phosphate buffered saline (PBS) to 480 ppm, was added to the first well of each row. Then using a multichannel pipette set to 100 µL, the CSA-SNP/MHB solution was serially diluted across, thus making each consecutive well 50% the concentration of the well preceding it. At this time 100 µL of the prepared inoculum was added to each well and the plate was incubated overnight. The MIC is defined as the most dilute concentration of an antimicrobial that will inhibit visible growth of a microbe after overnight incubation [2]. Each row should contain a live control/negative control, i.e. a well that contains no antimicrobial. Each row should also include a well consisting of only the pure MHB. This well should remain clear after incubation, thus ensuring that the MHB was not contaminated at any point in the study. These two controls also serve as a means of comparison for the treatment wells, one representing uninhibited growth and the other representing no growth. Minimum bactericidal concentration (MBC) was then determined using methods established by LJ.de Nooijer and Wallert and Provost Lab [3]. To each well of the 96 well plate with a concentration equal to or greater than that of the MIC, 40 µL, 5 ppm 3-(4,5-Dimethyl-2-thiazolyl)-2,5-diphenyl-2H-tetrazolium bromide (MTT) was added and the plate was incubating 4 hours at 37˚C. Any indication of color change from yellow to purple precipitate indicates viable bacteria. This can be confirmed by adding 150 µL MTT solvent to each well and measuring absorbance at 590nm;

deviation in absorbance from a no bacteria control will indicate viable bacteria are present. The most dilute concentration of antimicrobial agent that results in no viable bacteria is the MBC. All trials were run in triplicate.

3.2.9b Time-Kill Assay

The rate of antimicrobial activity of CSA-SNP against *S. aureus* and *E. coli* was examined using a time-kill assay modified from Isenberg [4]. The inoculum was prepared by mixing one loop of the desired bacteria in 10 mL of Mueller Hinton Broth (MHB), which was then incubated at 37˚ C overnight. This inoculum was found to be 1.6 x 10^8 cfu/mL by plating serial dilutions. For testing, inoculum was diluted to 1 x 10^6 cfu/mL, and used promptly that day. Next, 100 µL of inoculated broth was added to each well a 96 well plate. CSA-SNP suspended in deionized water was added so that the final concentration in each well was 5, 10, 20, or 30 ppm. Immediately after exposure, 10 µL alamarBlue (Invitrogen), as recommended by the producer, was added to one sample from each concentration; alamarBlue was sequentially added to the other wells at one hour intervals thereafter. A negative control, representing uninhibited growth, was also included with each time group; this control consisted of only bacteria in MHB at the diluted concentration. The absorbance of each sample was read three hours after exposure to alamarBlue using a Wallac 1420 Victor2 Multilabel Counter (Perkin Elmer). A 531 +/- 25 nm filter was used for excitation, and 593 +/- 60 nm was used for emission. All trials were done in triplicate.

3.2.10 Confocal Imaging

Spatial selectivity of the CSA-SNPs to *S. aureus* was visualized using Leica Microsystems DM IRE 2 confocal microscope system and corresponding software. *E.*

coli and *S. aureus* were cultured in Mueller-Hinton nutrient broth for 24 hours at 37°C. After incubation, *E. coli* and *S. aureus* were diluted to $1x10^7$ cfu/mL; dilutions were made in sterile Mueller-Hinton bacterial broth. Five hundred microliters of each dilution was then placed into the same well of a Lab-Tek II Chambered #1.5 German Coverglass System. The co-culture of bacteria was allowed to affix to the slide for 1 hour undisturbed. The solution was then removed. Next, the co-culture was exposed to CSA-SNP diluted into PBS+ Ca^{2+} and Mg^{2+} at 24 mg/L. The co-culture was exposed to the CSA-SNP on a wobble plate. This solution was removed after 30 minutes. The well was rinsed with 500 µL of PBS+ to remove excess nanoparticles. After the rinse was removed, the co-culture was stained with Life Technologies LIVE BacLight Bacteria Gram Stain Kit. In accordance with manufacturer's protocol, the stain was prepared by mixing 1.5 µL of BacLight component A (SYTO 9) and 1.5 µL of component B (hexidium iodide) into 500 µL of PBS - Ca^{2+} and Mg^{2+}. The bacteria were allowed to stain for 15 minutes in the dark, and then imaged using Leica Microsystems DM IRE 2 confocal microscope system and software.

3.2.11 Image Analysis

Quantitative analysis was performed on the confocal and TEM images using the Image Processing Toolbox in MATLAB (MathWorks, Natick, MA). For TEM analysis: grayscale images were converted to binary images with a threshold calculated by Otsu's method. After comparison with the original images, thresholds were manually adjusted if necessary. Binary morphological operations were performed to identify nanoparticles, which were then counted as groups of connected pixels. Finally, effective

diameters were estimated given a known area of pixels for each nanoparticle and assuming a circular cross-section; n=397 nanoparticles.

For quantitative confocal analysis, images from each imaging channel were read into MATLAB. A threshold was again calculated by Otsu's method and modified manually after comparison with the overlay of the three channels (due to differential uptake of each stain, cell morphology was used when necessary to aid in manual threshold determination). Next, the centroids of isolated objects (*S. aureus* cells, *E. coli*, and silver nanoparticles) in each channel were identified. Using the two-dimensional distance formula, the distance from the centroid of a single nanoparticle to the centroid of every *S. aureus* and *E. coli* was calculated; the minimum distance of those calculated for *S. aureus* and *E. coli* represents the closest of *S. aureus* and *E. coli*, respectively, to that nanoparticle. This process was repeated for each nanoparticle in the image. Statistical analysis, specifically student's t-test for significance and Ripley's K-function for clustering, were performed.

3.2.12 Optical Trapping

The instrument (MMI CellManipulator, MMI, Zurich, Switzerland) was fabricated to work as an optical trapping system with force measurement capabilities. The optical trapping laser used was an 8 W Nd: YAG (yttrium aluminum garnet) laser emitting light at a wavelength of 1070 nm. The laser beam used was expanded to maximally illuminate the back aperture of the microscope objective. The objective used was a 100X plan fluor objective (Nikon Instruments). A galvanometer was used that could create multiple individual traps simultaneously using a time-sharing mode. The instrument was designed as an optical trapping system using a Nikon TE2000 for

imaging. Also, for this study CSA functionalized microparticles (CSA-MP) were synthesized of polystyrene beads functionalized with a colloidal silver shell and CSA-124. These particles share the same surface chemistry as the CSA-SNP but are larger, typically 1 micron. This larger size facilitates optical capture and imaging.

A glass slide was passivated with dried milk, and a diluted sample of CSA-MP and *S. aureus* was placed on the surface. The slide was then sealed with a glass coverslip and parafilm. The slide was then placed under a 100x oil immersion objective and the laser turned on. Two traps were created, one for a single bacteria and another for a CSA-MP nanoparticle. The laser power was adjusted to about 30% to minimize potential spurious laser interactions and heating. The trap containing the bacteria was slowly moved to approach the *S. aureus* to eventual contact, as indicated by slight displacement of both. In this series of measurements the staph/CSA-NP adduct was annealed about 2 seconds before moving the traps apart. The same procedure was followed with identical beads that did not contain CSA-124. Results reported are based on an average of 200 trials repeated over 80 sets of independently prepared microscope slides.

3.3 Results and Discussion

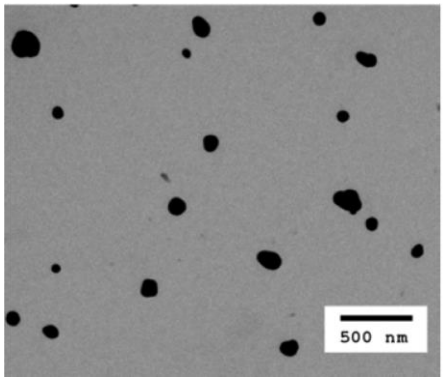

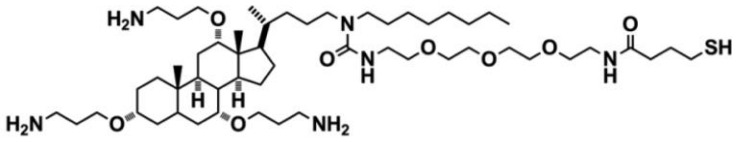

Figure 3.1. (Left) TEM of CSA-SNP and (right) CSA-124 structure.

Nanoparticle size was determined through TEM image analysis and DLS (Figure 3.1). These results are reported in Table 3.1. As expected, the hydrodynamic diameter determined via DLS is greater than the diameter determined via TEM due to the presence of solvated surfactant on the particle surface because the former is a weight-average technique. Also of note is that the hydrodynamic diameter increased as the positively charged.

Table 3.1. Nanoparticle characterization.

Parameter	HPC-SNP	CSA-SNP
SNP diameter via TEM analysis (nm)	68 +/- 18	64 +/- 38
Hydrodynamic diameter (nm)	81.9 +/- 9.4	102.2 +/- 2.3
Zeta potential (mV)	-18.23 +/- 0.83	-8.34 +/- 1.05

CSA-124 molecules were added to the system, indicating self-assembly on the nanoparticle surface. While precise size and distribution of CSA-SNPs are not critical in these experiments, they are relevant to colloidal stability and in vivo biocompatibility. Larger particles are more likely to settle from solution, potentially irreversibly aggregating and increasing apparent size. Also, nanoparticles possessing a diameter greater than 200 nm are more prone to activate the complement system and thus be cleared from the circulatory system [5]. Nanoparticles with a diameter under 100 nm are capable of penetrating blood vessel pores, and NPs under 20 nm can access interstitial spaces [6]. This characteristic has been termed the enhanced permeability and retention (EPR) effect [7].

As expected, the nanoparticle gains positive charge after the addition of CSA, due to the three ammonium groups on CSA-124 in neutral media. This data supports the fact that CSA was successfully conjugated to the nanoparticle surface. It is also relevant

because the nature of the surface charge also affects the nanoparticles' in vitro and in vivo interactions. Particles with a moderately neutral charge will be more likely to agglomerate, resulting in shorter shelf lives, a lower solubility threshold, and an increased probability of removal from in vivo circulation [8]. Once in the body, nanoparticles are susceptible to opsonization, recognition, and removal by the mononuclear phagocyte system (MPS). In general, neutral to negatively charged nanoparticles with hydrophilic polymer surfaces exhibit prolonged circulation times [5].

An appealing quality of the CSA-SNP is the ease of noble metal nanoparticle conjugation. CSA-124 has been specifically synthesized with a thiol-terminated polyethylene glycol side chain that favorably binds to noble metals. The SmartSilverAS silver nanoparticles, from this point referred to as SNPs, used for this procedure are stabilized with hydroxypropyl cellulose (HPC), which provides the nanoparticles with high solubility in aqueous and organic alcohol solvent systems and increases biocompatibility. Because CSA-124 has greater thermodynamic and steric stability than HPC on the surface of the SNPs, CSA-124 spontaneously displaces a portion of the HPC molecules.

For the quantification of CSA-124 bound to the SNP surface, we first constructed a standard curve of integrated peak area versus known CSA concentration using HPLC−ESI-TOF-MS. The CSA was displaced from the SNP surface using DTT; the particles were separated by centrifugation and analyzed using HPLC−ESI-TOF-MS. The corresponding CSA concentration was determined to be 1.5 mg/L for a 500 μL sample, or 4.52×10^{14} CSA molecules. Using ICP-OES and estimates of particle size from TEM, we

determined the same 500 μL sample contained 1.32×10^{11} SNPs, and thus, we conclude there are on average 3424 CSA- 124 molecules bound to each SNP.

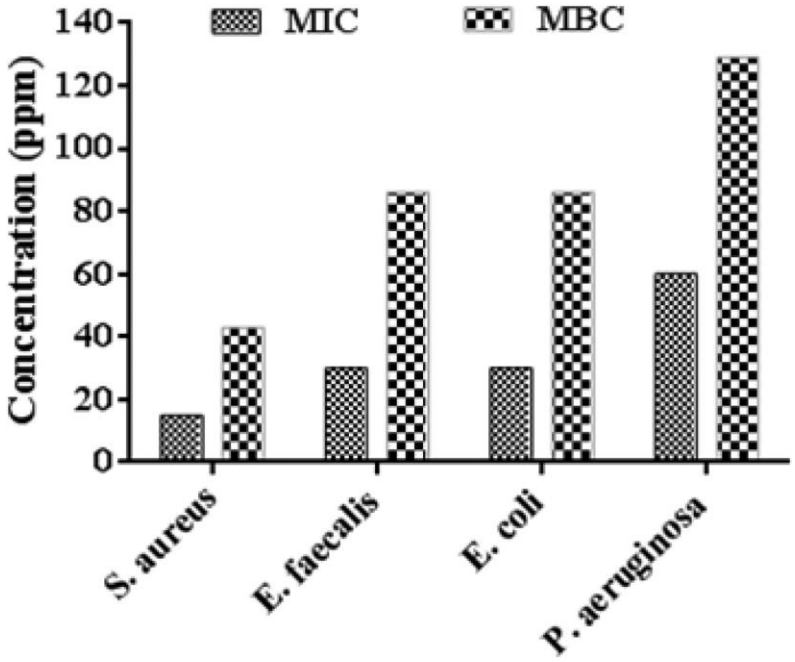

Figure 3.2. MIC and MBC of CSA-SNP against various bacteria.

The antimicrobial results for the minimum inhibitory concentration (MIC) and minimum bactericidal concentration (MBC) are reported in Figure 3.2. As the graph indicates, CSASNPs demonstrate similar efficacy against *S. aureus* (MIC 15 ppm), *E. faecalis* and *E. coli* (MIC 30 ppm), and *P. aeruginosa* (MIC 60 ppm). Our own determination of the MIC of SNPs was obtained using the same protocol as above and found to be roughly 250 ppm for both *S. aureus* and *E. coli*. While this study demonstrates that a CSA-SNP conjugate is a more potent antimicrobial than an SNP alone, it does not attempt to elucidate the mechanistic roles of each component, as potential mechanisms of each have previously been published. Antimicrobial properties of CSA have been attributed to membrane disruption through depolarization and permeabilization, while SNPs have been demonstrated to disrupt cell wall synthesis,

membrane ion pumps, translation, and nucleic acid synthesis [9-11]. Also of note, Kim et al. reported that SNPs alone inhibited *E. coli* 10 times more effectively than *S. aureus*, suggesting the CSA may impart SNPs with some mechanism of selectivity [12]. Further evidence of physical selectivity was given by confocal imaging of co-cultures of these bacteria. Statistical analysis using MATLAB demonstrated that CSA-SNPs were more likely to be near *S. aureus* than *E. coli*. This could be due in part to electrostatic attraction between the cationic CSA and the negatively charged peptidoglycan, which Gram-positive bacteria express in much greater quantities [13]. It has been well demonstrated that different cell types present different membrane constituents to its surrounding environment, which influences how the cell responds to extracellular foreign bodies, a concept known as cell vision. This phenomenon impacts the surface binding, cellular uptake, and internal fate of nanoparticles and in part explains the drastic differences in NP response among various cell types.

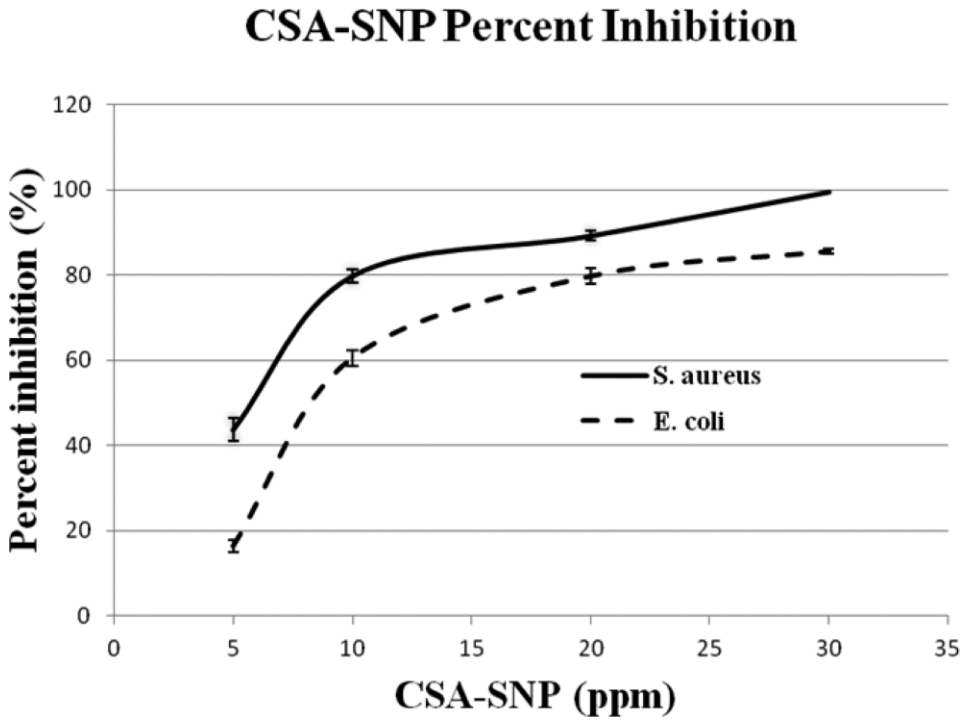

Figure 3.3. Time-kill assay showing increased inhibition of *S. aureus* versus *E. coli* due to CSA-SNPs. Percent inhibition is with respect to unexposed live controls.

Further antimicrobial characterization was provided through a time-kill study. As depicted in Figure 3.3, minimal inhibition is seen at 5 ppm, and efficacy increases as concentration increases. Note that inhibition results of the time-kill assay vary slightly from those of the MIC, as this was a 4 h study and MIC is a 24 h study. The results of the time-kill assay echo those of the MIC/MBC in that *S. aureus* shows increased sensitivity to CSA-SNPs compared to *E. coli*.

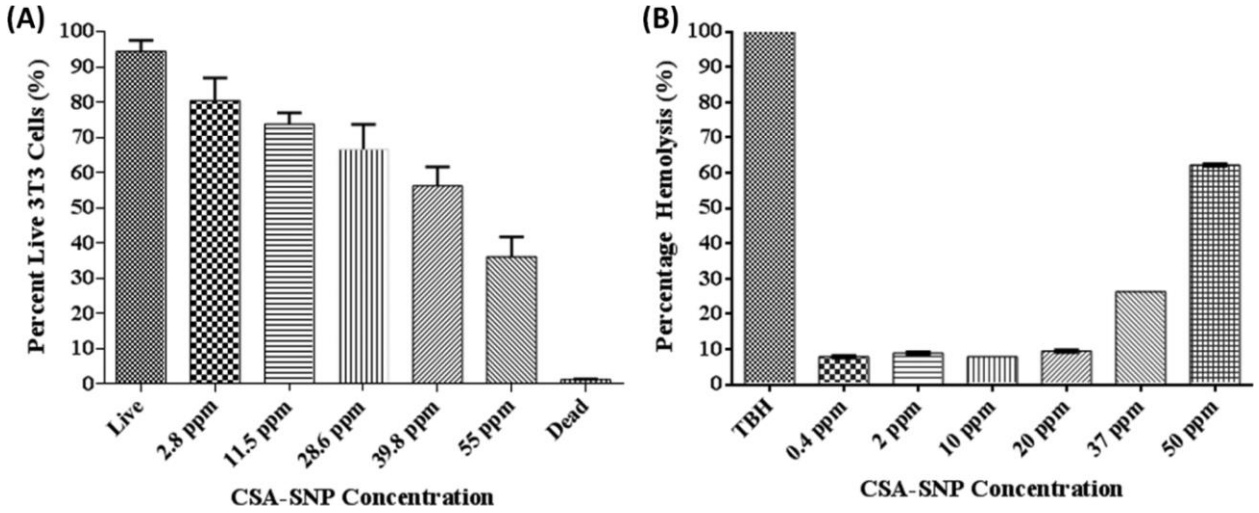

Figure 3.4. (A) Cytotoxicity of CSA-SNPs. (B) Hemolytic activity of CSA-SNPs.

The concentration dependent toxicity of CSA-SNPs to mouse 3T3 fibroblasts was determined by cell treatment followed by flow cytometry and is presented in Figure 3.4. The CSA-SNPs show very limited toxicity below 39.8 ppm and reach the 50% viability threshold at ~50 ppm. The differences between the live control and the 39.8 and 55 ppm samples were found to be significant by one-way ANOVA with Bonferroni's post-test ($p < 0.05$). The hemolytic assay shows nearly identical results with increasing hemolysis at 37.5 ppm and slightly over 50% hemolysis occurring at 50 ppm. The differences between the TBH, 37 ppm, and 50 ppm samples were found to be significant from all other

samples as determined by one-way ANOVA with Bonferroni's posttest ($p < 0.05$). These findings suggest about a 3-fold difference between MIC and EC50tox for *S. aureus* and 3T3 cells, respectively. Simultaneous testing of SNPs alone showed little cytotoxicity up to 200 ppm. This result is supported by the work of Jain et al., who reported that the IC50 for SNPs against Hep G2 cells to be 251 ppm. These findings suggest that CSA-SNPs are roughly 5 times more toxic to 3T3 cells than SNPs alone.

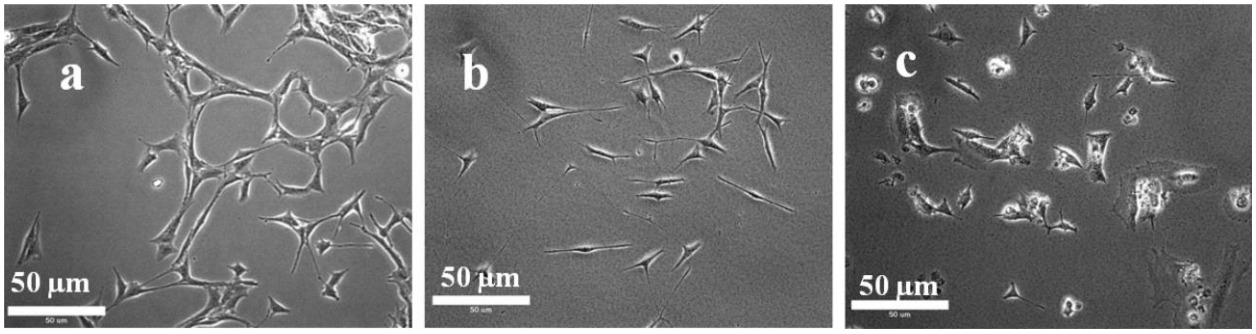

Figure 3.5. Bright-field images of 3T3 fibroblasts that received (a) 0 ppm, (b) 15 ppm, and (c) 37 ppm of CSA-SNP.

The cytotoxic effects of CSA-SNPs were also qualitatively assessed via bright-field imaging. In Figure 3.5a, the typical spindle morphology of healthy 3T3 fibroblast cells can be seen. In Figure 3.5b, representing the MIC of *S. aureus* at 15 ppm of CSA-SNP, the cells appear to have slightly reduced size but retain their characteristic spindle morphology. CSA-SNP at 37 ppm results in stark contrast in cell morphology indicative of cytotoxicity. These results are consistent with those from the hemolysis and flow cytometry studies.

Qualitative image analysis of the confocal overlays (Figure 3.6) suggests that the CSA-SNPs are distributed spatially closer to *S. aureus* cells than to *E. coli* cells. Analysis of these images provides the closest *S. aureus* and *E. coli* to each SNP; histograms and simple statistics are shown in Figure 3.7 and Table 3.2, respectively.

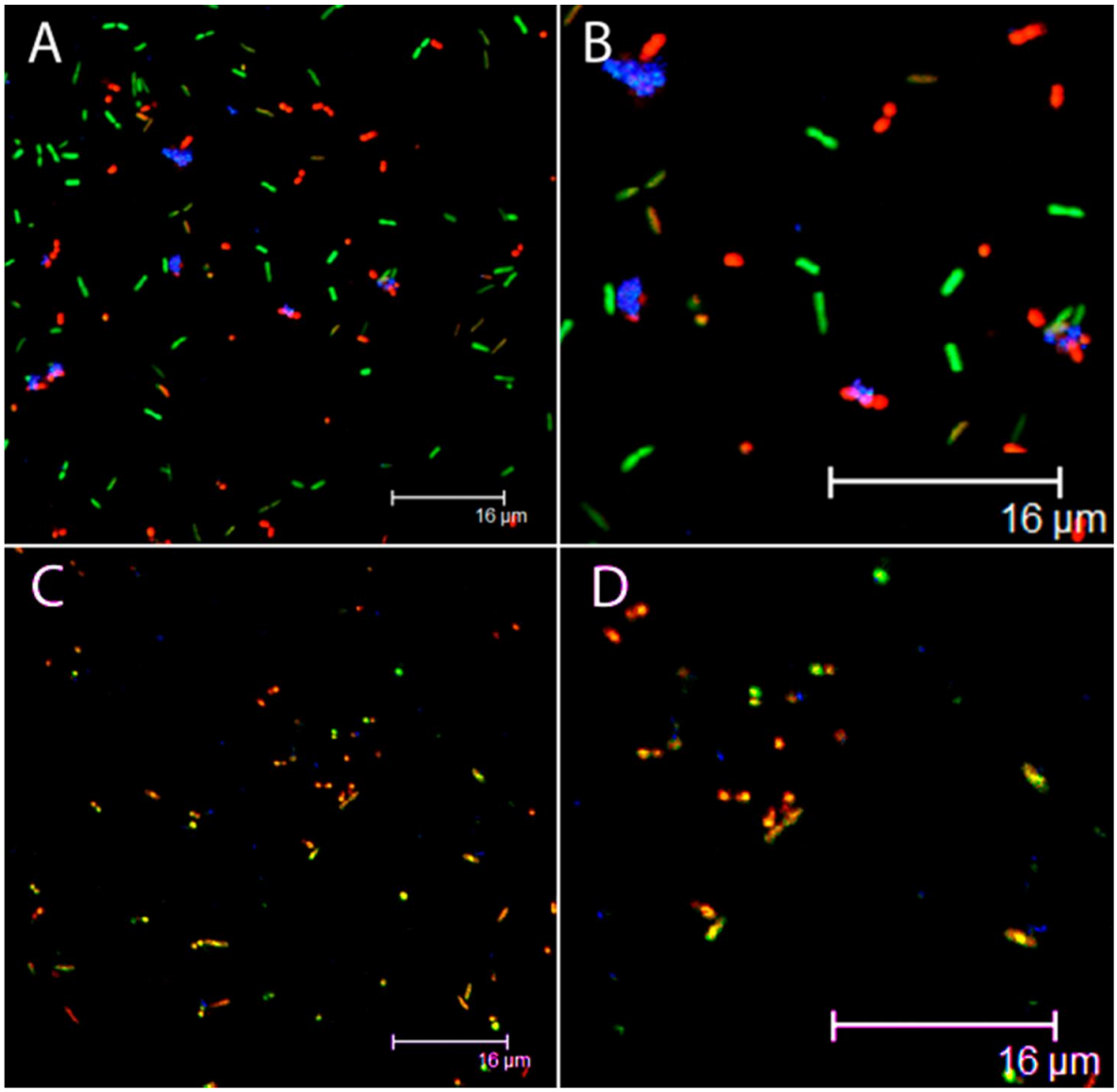

Figure 3.6. Confocal imaging of (red) *S. aureus*, (green) *E. coli*, and (blue) nanoparticles. (A and B) CSA-SNPs and (C and D) unmodified SNPs. (B and D) Enlarged segments of A and C, respectively.

Table 3.2 illustrates the distribution of distances for both experimental and negative control groups. The difference in average distance between CSA-SNP and *S. aureus* versus CSA-SNP and *E. coli* is statistically significant, as is the difference in average distance between the CSA-SNP treatment samples and the SNP negative control samples (two-way t test, $p < 0.05$). More than 70% of the CSA-SNPs are within 2 µm of

an *S. aureus* cell, whereas less than 40% of CSA-SNPs are within 2 μm of an *E. coli* cell. CSA-SNPs also show a higher incidence at distances greater than 5 μm from *E. coli* than from *S. aureus*. This is confirmed by the averages and standard deviations shown in Table 3.2; CSA-SNPs, on average, are closer to *S. aureus* than to *E. coli*. The standard deviations indicate less dispersion among the CSA-SNP to *S. aureus* data than the CSASNP to *E. coli* data. Ripley's K-function clustering analysis indicates that the CSA-SNPs are spatially clustered, particularly on shorter scales.

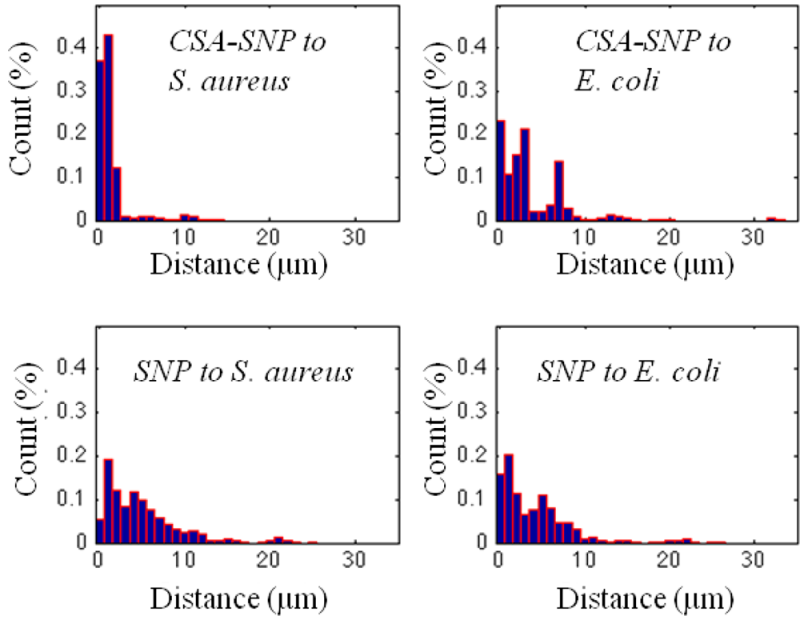

Figure 3.7. Histograms of (top) experimental and (bottom) negative control distances from SNPs to (left) *S. aureus* and (right) *E. coli*.

Table 3.2. Statistics from quantitative image analysis.

Samples	Avg. Distance from NP to Cell (μm)
CSA-SNP to *S. aureus*	1.283 +/- 1.994
CSA-SNP to *E. coli*	3.489 +/- 3.883
SNP (neg. control) to *S. aureus*	4.864 +/- 4.393
SNP (neg. control) to *E. coli*	3.991 +/- 4.165

The negative control data show no significant difference between the SNP to *S. aureus* distance and the SNP to *E. coli* distance. This is highlighted by large standard deviations for both negative control groups. However, statistically, the mean CSA-SNP to *S. aureus* distance is significantly different from the SNP to *S. aureus* average distance.

Selectivity was then qualitatively demonstrated on the scale of single cells through video observation and optical trapping technology. Optical trapping has the capability to manipulate small living biological objects, such as single bacterial cells, as well as inanimate particles. The infrared wavelength is minimally invasive to living cells. The optical trapping at a cellular level provides insight into biological interactions. Therefore, optical trapping of CSA-SNP and *S. aureus* was performed to further investigate the interactions and potential selectivity.

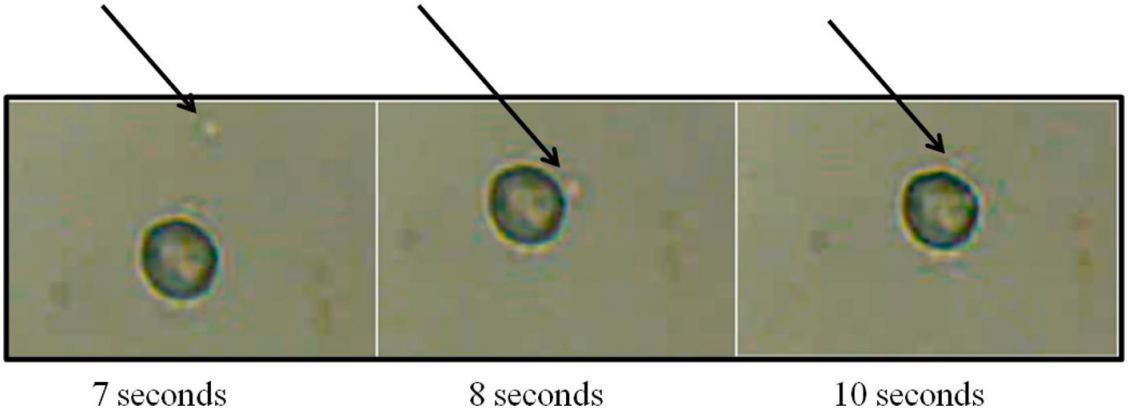

Figure 3.8. *S. aureus* (indicated with arrows) adhering to CSA-functionalized MP.

An optical trap was used to show the adhesion of CSA-MP to *S. aureus* (Figure 3.8). A single bacterium was trapped in one specific trap, and CSA-MP was simultaneously trapped in another trap. The bacteria were manually moved to approach the CSA-MP. The bacteria were then allowed to touch and reside for several seconds, and then the two traps were moved apart. The result was the *S. aureus* remained attached and was not able to be displaced by the force of the optical trap. The video shows that three

separate bacteria can attach and bind to one CSA functionalized particle. Repeated trials indicated that interactions generally formed within periods of <2 s. As a control, the procedure was repeated with nanoparticles lacking CSA-124 surfactant. The nanoparticles without CSA-124 did not manifest adhesion to *S. aureus*, even when extending the residence time beyond 10 s.

3.4 Conclusions

Silver has been used clinically as a broad-spectrum antimicrobial since it was approved by the FDA in the 1920s. Recent research indicates that there are many downsides to broad-spectrum antimicrobials including longer recovery times, increased risk of further infection, and higher incidence of drug resistance. The data presented suggest that the antimicrobial qualities of silver can be complemented via conjugation with selective ligands such as CSA-124. While SNPs alone have an MIC of 120 ppm against *S. aureus*, CSA-SNPs express an MIC of 15 and 30 ppm toward *S. aureus* and *E. faecalis*, respectively, and an MIC of 30 and 60 ppm toward *E. coli* and *P. aeruginosa*, respectively. This work further suggests that the functionalization of CSA to the nanoparticle surface imparts spatial selectivity in favor of *S. aureus* over *E. coli*; however, spatial selectivity does not necessarily imply antimicrobial selectivity. These findings were further supported through MATLAB analysis of confocal images, indicating that while in co-culture, 70% of CSA-SNPs were within 2 μm of an *S. aureus* cell while less than 40% were within 2 μm of an *E. coli* cell. Video images of laser captured nanoparticle interactions with both bacteria also show clear selectivity for the Gram-positive *S. aureus* over the Gram-negative *E. coli*.

3.5 References

1. International, A., *International Committee for Standardization in Hemotology*, in *Standard Test Method for Analysis f Hemolyti Properties of Nanoparticles*. 1979: West Conshohocken, PA.
2. Andrews, J.M., *Determination of minimum inhibitory concentrations.* Journal of antimicrobial Chemotherapy, 2001. **48**(suppl 1): p. 5-16.
3. Seligy, V. and J. Rancourt, *Antibiotic MIC/MBC analysis of Bacillus-based commercial insecticides: use of bioreduction and DNA-based assays.* Journal of Industrial Microbiology and Biotechnology, 1999. **22**(6): p. 565-574.
4. Isenberg, H.D., *Clinical Microbiology Procedures Handbook*. 2007, Washington, DC: ASM Press.
5. Perry, J.L., et al., *PEGylated PRINT nanoparticles: the impact of PEG density on protein binding, macrophage association, biodistribution, and pharmacokinetics.* Nano letters, 2012. **12**(10): p. 5304-5310.
6. Emerich, D.F. and C.G. Thanos, *The pinpoint promise of nanoparticle-based drug delivery and molecular diagnosis.* Biomolecular engineering, 2006. **23**(4): p. 171-184.
7. Chertok, B., et al., *Iron oxide nanoparticles as a drug delivery vehicle for MRI monitored magnetic targeting of brain tumors.* Biomaterials, 2008. **29**(4): p. 487-496.
8. Moghadam, B.Y., et al., *Role of nanoparticle surface functionality in the disruption of model cell membranes.* Langmuir, 2012. **28**(47): p. 16318-16326.
9. Monteiro, D.R., et al., *The growing importance of materials that prevent microbial adhesion: antimicrobial effect of medical devices containing silver.* International journal of antimicrobial agents, 2009. **34**(2): p. 103-110.
10. Chin, J.N., et al., *Potential synergy activity of the novel ceragenin, CSA-13, against clinical isolates of Pseudomonas aeruginosa, including multidrug-resistant P. aeruginosa.* Journal of antimicrobial chemotherapy, 2008. **61**(2): p. 365-370.
11. Leszczyńska, K., et al., *Bactericidal activities of the cationic steroid CSA-13 and the cathelicidin peptide LL-37 against Helicobacter pylori in simulated gastric juice.* BMC microbiology, 2009. **9**(1): p. 187.
12. Kim, J.S., et al., *Antimicrobial effects of silver nanoparticles.* Nanomedicine: Nanotechnology, Biology and Medicine, 2007. **3**(1): p. 95-101.
13. Morones, J.R., et al., *The bactericidal effect of silver nanoparticles.* Nanotechnology, 2005. **16**(10): p. 2346.

CHAPTER 4. ZEIN NANOPARTICLES AS A VEHICLE FOR OMEGA-3 FATTY ACID DELIVERY

4.1 Summary

Organic nanoparticles are useful in that they offer minimal cytotoxicity and can easily entrap payloads. This report details the synthesis and characterization of zein nanoparticles with entrapped docosahexaenoic acid and kept stable in solution by the surfactants lecithin and Pluonic F-127. The particles are produced using microfluidization at 30 000 psi and were found to be spherical in shape when examined with TEM. Dynamic light scattering reports a mean diameter of 124 nm ± 3 nm in fresh particles. The amount of DHA entrapped was quantified using gas chromatography and the synthesis was found to have a 76% entrapment efficiency. The particles were shown to have minimal cytotoxic effects towards 3T3 fibroblasts and particles with fluorescent FITC-zein were shown to associate with cells suggesting that they might increase uptake of their payload by cells.

4.2 Materials and Methods

4.2.1 Materials

The following materials were purchased from Sigma-Aldrich: zein from maize (Milkwaukee, WI), Pluronic® F-127 (Milkwaukee, WI), Docosahexaenoic acid (DHA) (>98% pure) (St. Louis, MO). The DHA was aliquotted into microcentrifuge tubes and stored under argon at -20°C after its initial opening; tubes were used one at a time for testing. Lecithin was purchased from Fischer Scientific. For cell culture, DMEM-RS, trypsin (0.25%, 1× solution), and DPBS/modified (1×) are HyClone products and are also ordered through ThermoScientific. Sytox Red dead cell stain was purchased from

Molecular Probes by Life Technologies Corporation. All other chemicals were used as received unless otherwise noted.

4.2.2 Nanoparticle Synthesis

Nanoparticles of DHA and zein were synthesized by a modification of the synthesis of Podaralla and Perumal [1]. Briefly, 10 mg/mL of zein were dissolved in a 70% (v/v) ethanol-aqueous solution. A solution of 0.75 mg/mL DHA was dissolved in 100% ethanol and added drop-wise to the zein solution under mild stirring in a 1:1 ratio. This mixture was injected into a solution containing 0.45% and 0.9% (w/v) lecithin and Pluronic F127, respectively (2:7.5 DHA/zein:Pluronic/lecithin solutions). The mixture was processed in a microfluidizer (M-11op, Microfluidics, MA, USA) for 3 cycles at 30,000 psi. The sample then underwent evaporation for 45 minutes under vacuum (500 mmHg) in a rotovapor (Buchi R-124, Buchi Analytics, DE, USA). After the ethanol was completely evaporated, the particles were purified via dialysis using a 100 kDa pore-size membrane (Spectrum Rancho, CA, USA) for 48 hours in deionized water to remove the Pluronic F127. The dialysis water was changed three times each day.

4.2.3 Transmission Electron Microscopy (TEM)

TEM images were obtained using a JOEL 2011 (Tokyo, Japan) to determine nanoparticle morphology. Nanoparticle solutions were diluted to approximately 30 ppm in DI water and 5 µL was applied to an Electron Microscopy Sciences carbon film 400 square mesh copper grid and allowed to settle for 2 minutes before excess water was removed. The grid was then stained with uranyl acetate for 30 seconds. Images were taken at 50-60,000X.

4.2.4 Dynamic Light Scattering (DLS) and Zeta Potential

Hydrodynamic diameters and Zeta Potential were measured using a Malvern Zetasizer nano series (Worcestershire, UK). Nanoparticles were diluted to approximately 1 ppm in DI water then filtered using a Thermo Scientific Nalgene 0.45 µm surfactant-free cellulose acetate membrane. Samples were measured in Malvern DTS1061 disposable capillary cells at 25°C.

4.2.5 Percent Yield

The percent yield of the process was determined by obtaining lyophilizing the nanoparticle solution in a Labcono FreeZone 2.5 Liter Casade Console Freeze Dry System (MO, USA). Vials used to hold the sample were weighed in triplicate while empty and again with the dried sample. A control with no DHA was also dried in triplicate to determine the mass of lecithin and Pluronic F127 remaining in the sample. The mass of the control was subtracted from the mass yield in determining the percent yield as according to the following equation:

$$Percent\ yield = \frac{Mass\ yield}{Theoretical\ mass\ yeild} \times 100\%$$

4.2.6 Gas Chromatography (GC)

The amount of DHA entrapped in the nanoparticles was determined by using a Varian CP-3800 gas chromatograph (Valnut Creek, CA, USA) coupled with a Saturn 2200 mass spectrometer. Samples were prepared as follows: dried sample was placed in a clean test tube with 2 mL of C17 solution in hexane at 100 ppm. The sample was vortexed to suspend it and sonicated for 15 minutes. Solids were removed by centrifugation (10,000g, 20 min) and the hexane layer collected and transferred to a new tube. The new tube was vacuum dried to and 2 mL of BCl_3 was added and vortexed. The

tube was placed in a 60°C water bath for 30 minutes, and subsequently placed in an ice bath for 10 minutes. One mL of water and 1 mL of hexane were added to the tube, vortexed, and let stabilize until phases separated. The upper layer of hexane was collected and placed in a new tube with sodium sulfate at the bottom to remove moisture. The hexane was then removed and transferred to a GC vial for determination. The drug entrapped was determined by the following equation:

$$Drug\ entrapment\ (\%) = \frac{Mass\ of\ drug\ in\ NP * 100}{Mass\ of\ drug\ used\ in\ formulation}$$

4.2.7 Thiobarbituric Acid Reactive Substances (TBARS) Assay

A TBARS assay kit was purchased from Cayman Chemical (item 10009055, MI, USA). A standard curve (R^2>0.99) was created using dilutions of MDA provided with the kit. Briefly, samples were prepared by pipetting 100 µL of nanoparticle solution at varying concentrations into a clean tube along with 100 µL of SDS provided in the kit. Next, 4 mL of Color Reagent was added to each vial; all vials were capped and then placed into vigorously boiling water for one hour and subsequently placed in an ice bath for 10 minutes to quench the reaction. One milliliter of solution from each vial was centrifuged at 1600 FCS at 4°C for 10 minutes. Within 20 minutes, 150 µL of solution was pipetted into a clear 96-well plate and read using a Wallac 1420 Victor2 Multilabel Counter (Perkin Elmer). A 531 +/- 25 nm filter was used to measure absorbance. All trials were done in triplicate.

4.2.8 Cytotoxicity Analysis

The effect of the nanoparticles on the metabolic activity of 3T3s was tested using alamarBlue (Invitrogen). The fibroblasts were seeded onto 96-well plates in 150 µL of

growth medium (DMEM, 10% FBS) and allowed to grow for until 80% confluent. The medium was then replaced with of medium containing incremental concentrations of zein-DHA nanoparticles suspended in growth medium. Live controls received 150 µL of the growth medium containing no nanoparticles. Dead controls received 150 µL of 100% ethanol 4 hours prior to alamarBlue exposure.

After 20 hours of exposure, 1.5 µL of alamarBlue was added to each well. After four hours, the media was read using a Wallac 1420 Victor2 Multilabel counter (Perkin Elmer). A 531 +/- 25 nm filter was used for excitation, and a 593 +/- 60 nm was used for emission. All trials were done in triplicate.

4.2.9 Cell Uptake

Nanoparticle uptake by 3T3 fibroblasts was qualitatively determined using fluorescently-labeled nanoparticles. Fluorescent zein was synthesized based on the reaction of the primary amines of the zein to form a covalent bond with fluorescein isothiocyanate (FITC). Two and a half grams of zein were placed in a round bottom flask and dissolved with 40 mL of dimethylformamide (DMF) at room temperature. Next, 25 µL of N,N-diisopropylethylamine (DIPEA) and 22 mg of FITC were added to the reaction flask. The mixture was kept at room temperature under stirring for 12 hours. Then, half of the DMF was evaporated with a Buchi rotavapor R-120 and the concentrated mixture was precipitated by addition of 60 mL dichoromethane (DCM). The light yellow solids were filtered out and resuspended in 20 mL of DMF. The sequence was repeated two times with DCM and two times with ether. The washing step to remove the free FITC was stopped when the supernatant solution was completely clear. Finally, the solids were dried in a high vacuum oven over night. The dry FITC-zein was stored at

4°C until use. The synthesis described in 4.2.2 was then used with the FITC-zein to yield fluorescent nanoparticles.

The cells were grown for 24 hours in 12-well plates in 500 µL of growth media until they were 70% confluent. After 24 hours, 100 µL of fluorescent nanoparticle solution at 50 ppm, filtered through a 0.45 µm a Thermo Scientific Nalgene surfactant-free cellulose acetate membrane, was added to each well, and the culture was incubated for 3 hours. The cells were then trypsinized, centrifuged at 1.8 rpm for 10 minutes. The cells were resuspended in 800 µL of DMEM (10% FBS, 1% triple antibiotic) and then re-plated into a 12-well plate containing a 18 mm glass coverslips (VWR, item 48282-041). The cells were allowed to affix for 4 hours before the media was aspirated and the cells were washed with 300 µL of room temperature PBS (-Ca,-Mg). Next, 100 µL of 2% PFA was added and allowed to affix the cells for 10 minutes. The coverslips were then removed and allowed to air dry. One drop of ProLong® Antifade Mounant (Life Technologies, item P36930) was added on the coverslip before it was placed on a microscope slide. The ProLong® was allowed to dry before the coverslip was permanently fixed to the slide.

The cells were imaged using a Leica DM RXA2 Deconvolution Microscope. A Differential Interference Contrast image was overlaid with a fluorescence image of the FITC (excitation 460-500 nm, emission 512-542 nm).

4.3 Results and Discussion

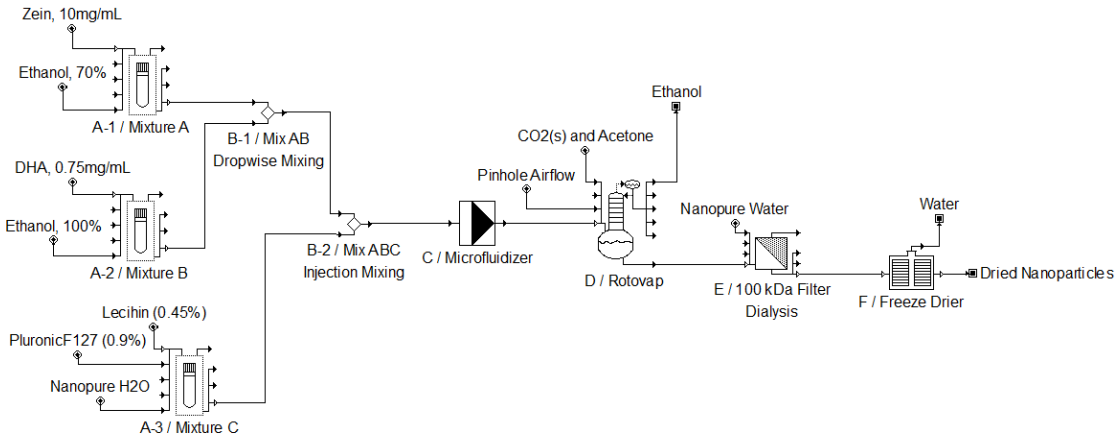

Figure 4.1 An overview of DHA-zein nanoparticle synthesis.

The process summarized in Figure 4.1 produced spherical nanoparticles of DHA and zein. The morphology was determined via TEM and uranyl acetate was used as a contrasting agent. Because the nanoparticles were hydrophobic, they readily took up the stain (Figure 4.2).

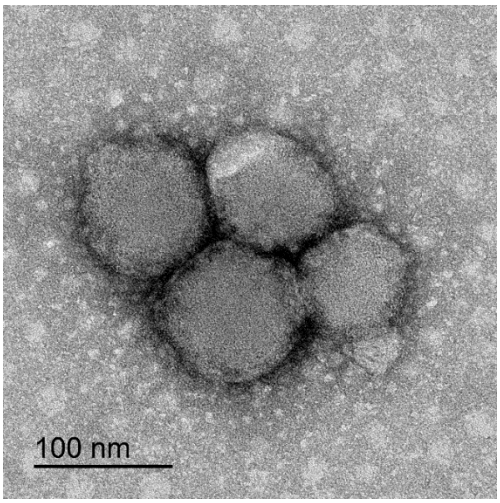

Figure 4.2. DHA-zein nanoparticles stained with uranyl acetate for contrast.

The size distribution of nanoparticles was determined by DLS. The emulation process produced a nanoparticles of the mean diameter of 124 nm +/- 3 nm. The particles produced a unimodal peak, and the sample was had a PDI of 0.208. The zeta potential

was determined to be -37 mV +/- 1 mV indicating that the emulsion is stable in solution. The small diameter of the particles indicates that they are more likely to be taken up by cells [2,3].

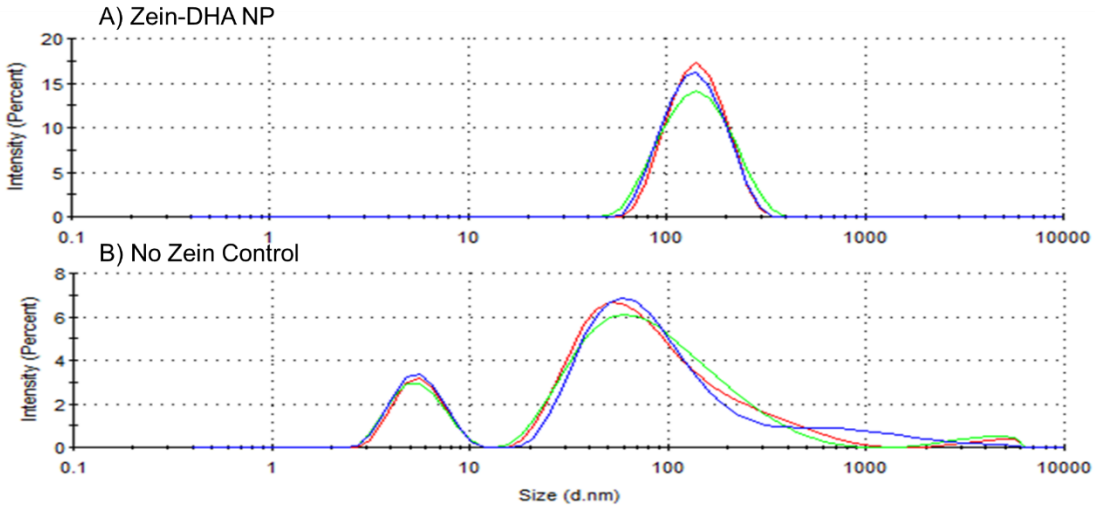

Figure 4.3. Intensity versus size curves from DLS of nano-emulsions. A) The size distribution of DHA-zein NPs produced is monodisperse around a single peak. B) A control group without zein shows the zein is a necessary component for monodisperse and stable nanoparticles.

In order to determine the effects of zein on the nanoparticles, a synthesis was performed without the addition of zein. The solution was interrogated using TEM (not shown) and DLS. As can be seen in Figure 4.3B, the resulting solution contains several peaks of non-uniform particles; the PDI was found to be 0.713 indicated a very polydisperse suspension. This strongly suggests that zein is necessary for forming uniform particle size.

The mass recovered from three syntheses run at ten times scale was averaged and found to be 378.7 mg. This is approximately equal to the mass of the inputs to the synthesis minus the Pluronic F127. This indicates that the dialysis step was effective in

removing the Pluronic F127 while retaining the other components of the synthesis. The percent yield excluding the mass of Pluronic was determined to be 85% ± 12%.

The amount of DHA entrapped in the particles was quantified via GC. Sixty milliliters of NP solution was aliquotted into six equal parts and dried via lyophilization. The amount of DHA in the dried NP powder was found to be 4.548 mg; with the theoretical yield of 6 mg, the entrapment efficiency of the synthesis is 75.8%. Dividing the mass of DHA entrapped by the total amount of solid shows that the drug content (m/m) is 2.2%. Future testing will focus on the optimizing the loading of the DHA into the particles.

Because DHA readily oxidizes under ambient conditions, it is necessary to measure the oxidative stability of any products containing the fatty acid. Because of nanomaterials' increased surface area to volume rations, this problem is exacerbated when DHA is used nanoparticles. The oxidative resistance of the zein-DHA nanoparticles was tested via a TBARS Assay using one hour of boiling as an oxidative stress. The TBARS assay measures the production of malondialdehyde (MDA), a byproduct of lipid peroxidation via a colorimetric assay. A standard curve (R^2>0.99) was created using serial dilutions of pure MDA. The equation of this curve was used to calculate the amount of MDA produced by samples of nanoparticles and pure DHA with equal concentrations of DHA in both the nanoparticle and pure samples (Figure 4.4). The results show that the amount of oxidation in the nanoparticles is no worse than pure DHA at the concentrations tested. This suggests that DHA in the particles will have approximately the same shelf life as DHA solutions.

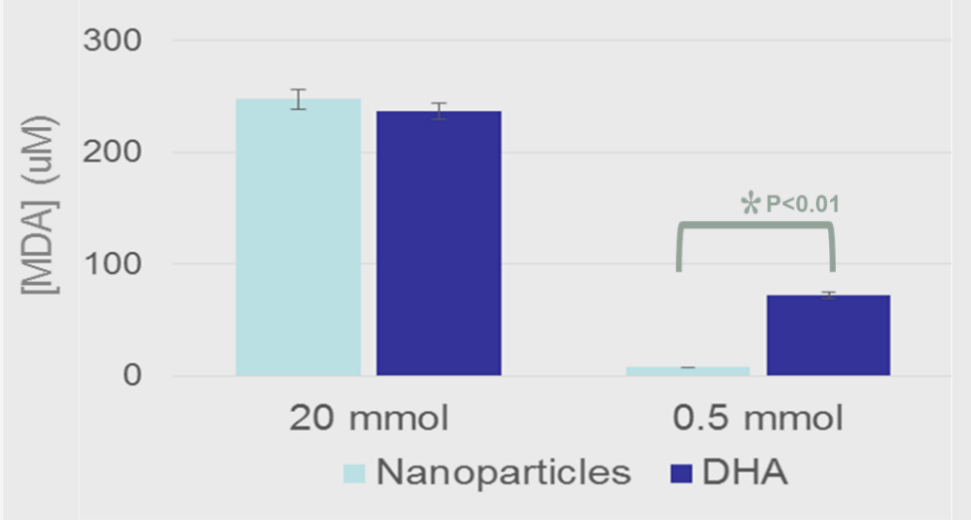

Figure 4.4. The oxidative profile of DHA-zein NP compared to pure DHA at concentrations of 20 and 0.5 mmol of DHA.

The cytotoxicity of the particles against 3T3 fibroblasts was measured using an alamarBlue assay (Figure 4.5). This assay measures the amount of a fluorescent product produced when the cells metabolize the alamarBlue. The nanoparticles were dried and resuspended in DMEM (10% FBS, 1% antibiotic). This suspension was then filtered through a 0.22 μm pore filter to sterilze the sample before exposing to the cells. Figure 4.5 shows no appreciable decrease in cell viability up to 1000 ppm NP compared to a live control. The increased metabolic activity at 1000 ppm may be attributed to the cells trying to metabolize the zein found in the nanoparticles. Future testing will use a live/dead stain to further examine the biocompatibility of the nanoparticles.

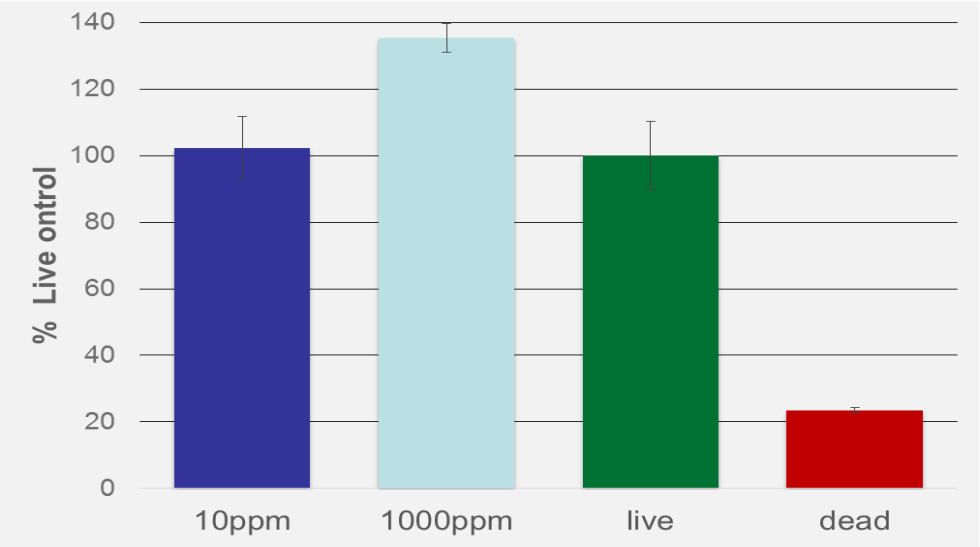

Figure 4.5. There is no decrease in cell viability up to 1000 ppm DHA-zein NP.

The ability of the nanoparticles to associate with mammalian cells was studied using nanoparticles synthesized with zein that had FITC coupled to it. The cells were exposed to the fluorescent nanoparticles for three hours at 37°C before being lifted from the plate using trypsin and washed by centrifugation. The cells were allowed to fix to a glass coverslip for four hours before being fixed with PFA. Figure 4.6 shows areas of fluorescent intensity (indicated by red arrows0 found only on the cells. This suggests that the particles are associating with the cells and may help increase the uptake of the DHA payload. Future testing will examine the uptake of the particles more fully and using different cell lines.

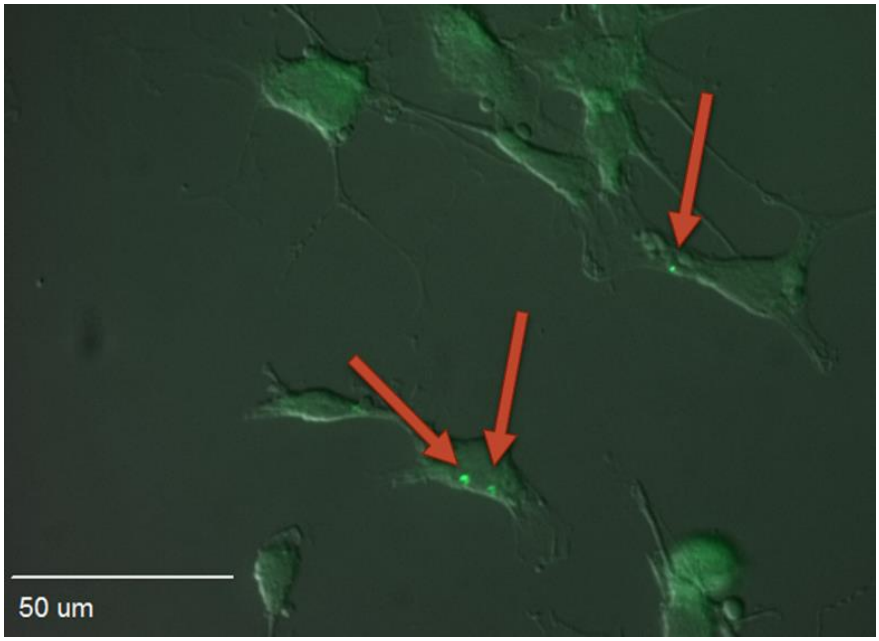

Figure 4.6. Nanoparticles with FITC-zein (red arrows) associate with 3T3 fibroblasts suggesting they may help increase uptake of the DHA payload *in vivo*.

4.4 Conclusions

A process to produce nano-sized particles with entrapped DHA was successfully designed using microfluidization. These particles can be successfully dried and suspended in aqueous solutions. The particles were able to be synthesized with an 85% yield and 76% entrapment efficiency. These particles associate with mammalian cells suggesting that they will improve uptake of DHA. Other research has implicated DHA in increased recovery time after traumatic brain injuries or stroke. Initial cell viability tests show that the particles do not produce significant cytotoxicity when measured with an alamarBlue assay. Future work will include optimization of DHA loading efficiency, live/dead staining of cells, hemolytic characterization, FACS with FITC-labelled zein, hemolytic characterization to test feasibility of intravenous injection.

4.5 References

1. Podaralla, S. and O. Perumal, *Influence of formulation factors on the preparation of zein nanoparticles.* Aaps Pharmscitech, 2012. **13**(3): p. 919-927.
2. Perry, J.L., et al., *PEGylated PRINT nanoparticles: the impact of PEG density on protein binding, macrophage association, biodistribution, and pharmacokinetics.* Nano letters, 2012. **12**(10): p. 5304-5310.
3. Chertok, B., et al., *Iron oxide nanoparticles as a drug delivery vehicle for MRI monitored magnetic targeting of brain tumors.* Biomaterials, 2008. **29**(4): p. 487-496.

CHAPTER 5. CONCLUSIONS

5.1 CSA-124 Conclusions

CSA-124 is an effective antimicrobial, and imparts spatiotemporal selectivity to nanoparticles to which it is conjugated via a silver-thiol bond. However, it fails to impart significant antimicrobial qualities to the DANs described in Chapter 2, and over a 24 hour study imparts only some antimicrobial selectivity to conjugated SNPs. Additionally, the cytotoxic and hemolytic qualities of CSA-SNPs, described in Chapter 3, make CSA-124 a less desirable choice for further testing.

Despite their high cost, artificially synthesized replicated of naturally occurring peptides are worth reviewing as a viable method of developing new antimicrobials. Some antimicrobial peptides have been shown to be highly efficacious with either a very low MBC, a specific microbial target, or both. For some of these peptides, the specific part of the sequence which imparts its antimicrobial effects has been identified. These truncate sequences can greatly reduce the cost of synthesis and thus the viability of testing antimicrobial peptides for use as clinical agents.

Another obstacle to the effective experimentation of antimicrobial peptides is the lack of high throughput testing methods. The large quantities peptide and other materials required to determine the effects of peptides towards different microbial species greatly increases the cost of experimentation. One method to overcome this could lie in a technique currently used with great success in gene expression studies: micro-plotting. Micro-plotters use extremely small quantities of sample and can place thousands of replicates on the area of a single microscope slide. In gene expression studies, print samples with a fluorescent reporter onto a microscope slide. The intensity of the reporter

can be used to determine the amount of expression of a particular set of genes being tested or of the entire genome of a cell.

With regards to peptides, this technique could be used in a similar manner. Lesaicherre et al. describe a reaction which allows for the attachment of peptides to an epoxide-treated glass slide via the N-terminus [1]. Many antimicrobial peptides are active at their C-terminus [2], and moreover, peptides can be attached to nanoparticles by their N-terminus via EDC chemistry described by Sarfati et al. [3]. Thus, peptides can be attached to glass slides via a microplotter in a similar orientation to the way in which they can be attached to nanoparticles. Such slides were developed in a pilot study to determine the viability of this method as a high throughput method of testing peptides for antimicrobial qualities. The proteins were synthesized with a fluorescent reporter (FMOC (Lys 5/6 FAM)) so that they could be imaged via fluorescent microscopy. Bacteria were labeled with DAPI (Figure 5.1). Further statistical analysis is necessary to determine the means by which peptides can be selected via this method.

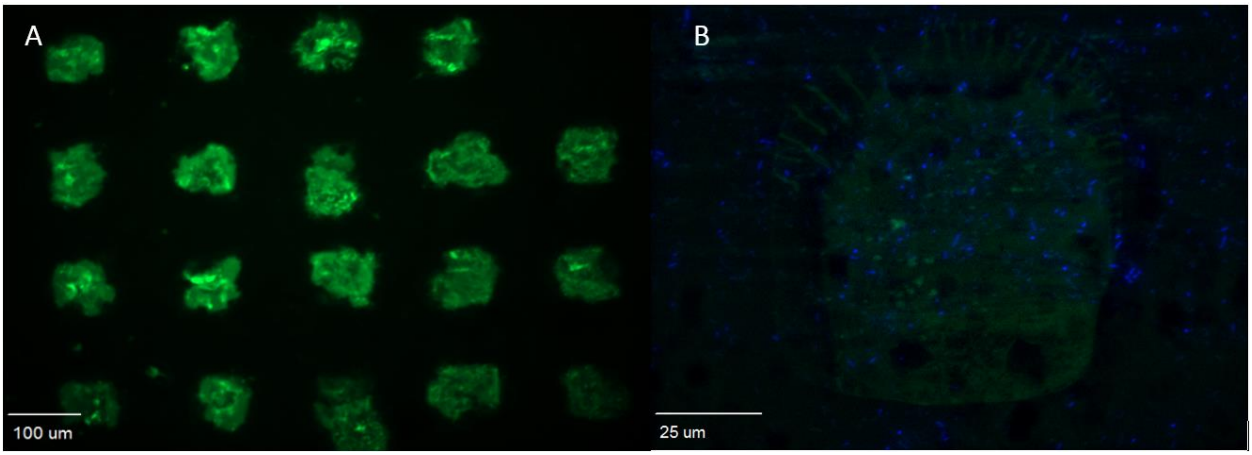

Figure 5.1. (A) A microarray of FMOC labeled peptides. (B) DAPI (blue) labeled bacteria over a single microspot.

5.2 Zein-DHA NP Conclusions

The particles made of DHA and zein show promise as candidates for further testing. The particles are stable in solution, successfully entrap DHA, and associate with mammalian cells. Their ability to associate with cells should be examined more in depth to determine if they truly help to increase with particle uptake. This uptake study should be examined with multiple cell types. Fluorescently activated cell sorting and fluorescent microscopy with multiple stains can be used as further evidence that particles are in fact being absorbed by the cells. The biocompatibility testing should also be expanded using a live/dead assay and hemolytic characterization to investigate the possibility of their use as an intravenous drug. Finally, pending the success of these tests, the particles should be studied in an *in vivo* model with both ischemic brain injuries and stroke models.

5.3 References

1. Lesaicherre, M.-L., et al., *Developing site-specific immobilization strategies of peptides in a microarray.* Bioorganic & medicinal chemistry letters, 2002. **12**(16): p. 2079-2083.
2. Bulet, P., et al., *Antimicrobial peptides in insects; structure and function.* Developmental & Comparative Immunology, 1999. **23**(4): p. 329-344.
3. Sarfati, G., et al., *Targeting of polymeric nanoparticles to lung metastases by surface-attachment of YIGSR peptide from laminin.* Biomaterials, 2011. **32**(1): p. 152-161.